



The Impact of Alternative Fuels on U.S. Domestic Aviation Emissions

Matteo Guidotti*, Rohit Gupta†, Jared Dost‡, Dhairy Mehta‡, Aadit Kolar‡, Christopher Zhang‡,
Phillip J. Ansell§, and Matthew A. Clarke¶
University of Illinois Urbana-Champaign, Urbana, IL 61801

The transition to alternative energy carriers offers a promising pathway to reduce the environmental footprint of aviation. This study investigates the impact of replacing conventional jet fuel with Liquid Hydrogen (LH₂), Liquefied Petroleum Gas (LPG), and Liquefied Natural Gas (LNG) across five representative classes of transport aircraft operating within the U.S. domestic network. To isolate the effects of fuel utilization, the analysis assumes fixed aircraft weight and performance, and focuses on direct operational emissions. Mission simulations are performed utilizing RCAIDE, a multifidelity preliminary aircraft design framework, while emissions are estimated through a Chemical Reactor Network (CRN) model representing a Rich-Burn, Quick-Mix, Lean-Burn (RQL) combustor. The study captures operational trends for each aircraft-fuel combination and quantifies the influence of alternative fuel properties on combustor-level and mission-level emissions. Results reveal trends associated with each energy carrier and emphasize the role of their specific properties in shaping direct emissions at the fleet level. These findings aim to offer insights into the challenges and opportunities associated with integrating alternative fuels into the existing U.S. domestic aviation network.

Nomenclature

Acronyms

AIC	Aviation Induced Cloudiness	LES	Large Eddy Simulation
BTS	Bureau of Transportation Statistics	LH ₂	Liquid Hydrogen
CFD	Computational Fluid Dynamics	LNG	Liquefied Natural Gas
CRN	Chemical Reactor Network	LPG	Liquefied Petroleum Gas
DA	Dilution Air	MJ/RPK	Megajoules per Revenue Passenger Kilometer
EASA	European Union Aviation Safety Agency	MTOW	Maximum Takeoff Weight
EI	Emission Index	NC12H26	Dodecane (normal)
FAA	Federal Aviation Administration	NPBENZ	n-Propylbenzene
FAMEs	Fatty Acid Methyl Esters	OEW	Operating Empty Weight
FM	Fast Mixing	PFR	Plug Flow Reactor
FAR	Fuel-to-Air ratio	PSR	Perfectly Stirred Reactor
FAR _{st}	Stoichiometric Fuel-to-Air ratio	PZ	Primary Zone
GSP	Gas Turbine Simulation Program	RCAIDE	Research Community Aerospace Interdisciplinary Design Environment
GWP ₁₀₀	100-year Global Warming Potential	RQL	Rich-burn, Quick-mix, Lean-burn
ICAO	International Civil Aviation Organization		
LHV	Lower Heating Value		

* Graduate Student, Department of Aerospace Engineering, AIAA Student Member.

† Research Associate, Department of Aerospace Engineering, AIAA Student Member.

‡ Undergraduate Student, Department of Aerospace Engineering.

§ Associate Professor, Department of Aerospace Engineering, AIAA Associate Fellow.

¶ Assistant Professor, Department of Aerospace Engineering, AIAA Member.

Acronyms (continued)

SA	Secondary Air	TIT	Turbine Inlet Temperature
SM	Slow Mixing	TMBENZ	Trimethylbenzene
SoI	System of Interest	TSFC	Thrust Specific Fuel Consumption
SoS	System of Systems	gCO ₂ e/RPK	Grams of CO ₂ -equivalent per Revenue Passenger Kilometer
SZ	Secondary Zone		

Symbols

A_{SZ}	Cross-sectional area of Secondary Zone [m ²]	$\dot{m}_{fuel,j}$	Fuel mass flow rate at thrust level j [kg/s]
c_p	Specific heat at constant pressure [J/(kg·K)]	$\dot{m}_{fuel,takeoff}$	Fuel mass flow rate at takeoff [kg/s]
$f(\phi_i)$	Mass flow distribution across PSRs as a function of local equivalence ratio	$\dot{m}_{air,j}$	Air mass flow rate at thrust level j [kg/s]
$f_{air,PZ}$	Fraction of total air directed to the Primary Zone	$\dot{m}_{air,takeoff}$	Air mass flow rate at takeoff [kg/s]
$f_{air,SA}$	Fraction of air directed to Secondary Air injection	$\dot{\omega}_k$	Molar production rate of species k [kmol/(m ³ ·s)]
$f_{air,DA}$	Fraction of air directed to Dilution Air injection	ϕ	Equivalence ratio
f_{SM}	Fraction of secondary air entering via Slow Mixing path	$\bar{\phi}$	Mean equivalence ratio
f_{FM}	Fraction of secondary air entering via Fast Mixing path	ϕ_i	Equivalence ratio in reactor i
h_k	Specific enthalpy of species k [J/kg]	$\phi_{PZ,des}$	Design equivalence ratio in the Primary Zone
h_{mix}	Enthalpy of fuel-air mixture at combustor inlet [J/kg]	$\phi_{SZ,des}$	Design equivalence ratio in the Secondary Zone
h_{air,P_3T_3}	Specific enthalpy of air at station 3 [J/kg]	$\Delta\phi$	Bin width for equivalence ratio distribution
h_{fuel,P_3T_3}	Specific enthalpy of fuel at station 3 [J/kg]	ρ_{gas}	Gas density [kg/m ³]
K	Number of chemical species	S_{PZ}	Mixing index in the Primary Zone
K_v	Pressure-flow tuning coefficient [kg/(s·Pa)]	T	Gas temperature [K]
L	Latent heat of vaporization [J/kg]	T_3	Temperature at station 3 [K]
L_{SZ}	Total axial length of the Secondary Zone [m]	TIT	Turbine Inlet Temperature [K]
$l_{SA,SM}$	Normalized length for Slow Mixing secondary air injection [-]	$t_{res,i}$	Residence time in reactor i [s]
$l_{SA,FM}$	Normalized length for Fast Mixing secondary air injection [-]	u	Axial gas velocity [m/s]
$l_{DA,start}$	Normalized start location of Dilution Air injection [-]	U	Heat transfer coefficient [W/(m·K)]
$l_{DA,end}$	Normalized end location of Dilution Air injection [-]	V_{PZ}	Volume of the Primary Zone [m ³]
m	Mass of reactor contents [kg]	$V_{PZ,i}$	Volume of reactor i in the Primary Zone [m ³]
\dot{m}	Mass flow rate [kg/s]	W_k	Molecular weight of species k [kg/kmol]
\dot{m}_{gas}	Mass flow rate of gas mixture in the SZ [kg/s]	Y_k	Mass fraction of species k
$\dot{m}_{k,gen}$	Mass generation rate of species k [kg/s]	$Y_{k,in}$	Inlet mass fraction of species k
		Δh	Enthalpy increase of fuel from standard to inlet conditions [J/kg]
		$\beta_{air,in}$	Axial air injection rate per unit length [kg/(s·m)]
		$\beta_{SA,SM}$	Axial air injection rate in SM path [kg/(s·m)]
		$\beta_{SA,FM}$	Axial air injection rate in FM path [kg/(s·m)]
		β_{DA}	Axial air injection rate in dilution segment [kg/(s·m)]

I. Introduction

AVIATION accounts for approximately 2.5% of the 35 billion metric tons of anthropogenic carbon dioxide (CO_2) emitted annually [1–3]. While this share may appear modest, it warrants close attention for several critical reasons. First, aircraft emissions exert a long-lasting impact on both the environment and human health. Aviation-related air pollution is estimated to cause approximately 16,000 annual premature deaths globally [3–5]. Second, although the aviation industry has achieved significant operational and technological improvements, surpassing its own target with an average annual fuel efficiency gain of 2.1% [6], these advancements may not be sufficient. Progress has been driven by innovations such as lightweight composite materials [7], improved aerodynamics [8], and optimized air traffic management systems [9]. However, the anticipated growth in global air traffic, projected at an average annual rate of 5.2% [1], risks outpacing these efficiency gains. As a result, total emissions from aviation are expected to increase significantly, with forecasts suggesting up to 2000 megatonnes of CO_2 by 2050 [10]. Third, aircraft emit a variety of greenhouse gases (GHGs) and other combustion products, beyond carbon dioxide. These include carbon monoxide (CO), water vapor (H_2O), unburned hydrocarbons (UHC), nitrogen oxides (NO_x), sulfur oxides (SO_x), and non-volatile particulate matter (nvPM, primarily carbon soot) [11, 12]. These emissions contribute to secondary environmental effects, such as Aviation-Induced Cloudiness (AIC), and their impact varies depending on engine operating conditions. For instance, nitrogen oxides are produced in greater quantities during high-thrust phases such as takeoff and climb [13]. In response, regulatory entities have intensified their efforts to mitigate the impact of aviation emissions, particularly around airports. The International Civil Aviation Organization (ICAO) has established standards targeting pollutants from landing and takeoff (LTO) cycles, including limits on UHC, CO, NO_x , and nvPM emissions [14].

The development of sustainable energy systems for aviation is further challenged by the aggressive power and energy requirements required for aerial transportation and the long, complex value stream inherent to renewable fuel production. To determine the full impact of an alternative energy system on sustainability goals, the full well-to-wake life cycle must be considered, including the production and supply components (well-to-tank) and direct operational (tank-to-wake) impacts. The sensitivity of flight efficiency to weight severely limits the direct application of battery-electric systems to displacing the energy requirements for most transport-class aircraft missions, and the lofty safety requirements of aircraft operation complicate the integration process of new energy systems. Nevertheless, exploring the substitution of conventional Jet A/Jet A-1 with low-carbon or carbon-free fuels remains a promising pathway towards decarbonizing aviation. In particular, several prospective fuels can be renewably produced by way of green hydrogen and captured carbon sources, including Liquid Hydrogen (LH_2), Liquefied Natural Gas (LNG), Liquefied Petroleum Gas (LPG), and Power-to-Liquid Synthetic Kerosene (PtL – SAF). However, the sustainability impact of alternative energy carriers also reaches beyond the in-flight emissions produced by a given aircraft. The economic feasibility and environmental impact of these energy carriers are primarily driven by the renewability of feedstocks used in renewable fuel production, as well as the overall efficiency of catalytic fuel production processes. As many of these environmental and economic outcomes will scale relative to production energy requirements, this parameter will be used as a general representation of well-to-tank efficacy.

This study presents an energy-based analysis aimed at evaluating the impact of replacing conventional jet fuel with LH_2 , LNG, and LPG. While previous research has explored the isolated properties and performance characteristics of alternative aviation fuels [15], little focus has been dedicated to their integration at the fleet level and their operational implications across representative mission profiles. To address this gap, this study utilizes five representative aircraft that can collectively be employed to approximate U.S. civil aviation operations to meet the following objectives:

- Quantify the energy requirements and direct emissions associated with the production and combustion of selected alternative fuels.
- Integrate a high-fidelity Chemical Reactor Network (CRN) model of a Rich-Burn, Quick-Mix, Lean-Burn (RQL) combustor, developed in Cantera [16], into an aircraft simulation environment to simulate fuel-specific emissions under representative engine operating conditions.
- Conduct trade studies across various aircraft-fuel combinations to evaluate the impact of fuel properties on both combustor-level and mission-level emissions.
- Provide insights into the challenges and potential benefits associated with the deployment of alternative energy carriers in the existing U.S. domestic aviation fleet.

In this study, aircraft configuration, weight, and performance are held constant across all scenarios to isolate the impact of fuel-specific properties on direct operational emissions. It is also assumed that the energy required to complete a given mission remains unchanged across all fuel types.

This paper is organized into four main sections. Section II provides a review of alternative energy carriers and discusses how their production pathways affect energy demand and emissions. It also introduces and explains the

specific alternative fuels selected for this study. Section III outlines the computational methodology used to quantify the direct flight emissions from domestic operations. Section IV summarizes the effects of a blanket adoption of each energy carrier onboard all classes of transport aircraft instantaneously. This section also includes a sensitivity analysis on combustion conditions to ensure consistency across all fuel types. Finally, Section V summarizes the key findings and conclusions.

II. A Review of Liquid-State Alternative Energy Sources in Aviation

To date, no single alternative energy carrier has emerged as the definitive solution for decarbonizing aviation. A wide range of candidates, each with distinct physical properties, energy densities, and combustion characteristics, are currently under consideration. For practical feasibility, this study focuses on liquid-phase energy carriers, including both conventional and cryogenic fuels. While cryogenic fuels such as liquid hydrogen offer high specific energy and low combustion emissions, they also introduce significant challenges related to storage, handling, and integration into existing infrastructure. Importantly, the total energy demand and greenhouse gas (GHG) emissions associated with fuel production are heavily dependent on the chosen production pathway. Moreover, the adoption of any alternative fuel requires compatible infrastructure for production, distribution, and refueling at scale. Several of the possible alternative fuels exist in a gaseous state under standard atmospheric conditions, which introduces additional engineering challenges for aviation applications. If these fuels are to be utilized effectively, advances in cryogenic technologies or high-pressure fuel tank systems will be essential to enable safe and efficient storage, transport, and onboard integration. A selection of pure fuels and fuel mixtures is summarized in Table 1, where Jet A/A-1 is included as a baseline for comparison.

Table 1 Liquid-state energy sources for aviation. [17] [18] [19]

Category	Fuel	Chemical Composition	Liquid Density [kg/m ³]	Specific Energy [MJ/kg]	Energy Density [MJ/L]
Non-Cryogenic	Jet A/A-1 (kerosene)	C ₈ –C ₁₆ hydrocarbons	804 at 288.15 K, 1 atm	43.2	34.7
	Ethane	C ₂ H ₆	546 at 184.55 K, 1 atm	47.8	26.1
	Propane	C ₃ H ₈	493 at 231.05 K, 1 atm	46.4	22.8
	Methanol	CH ₃ OH	792 at 293.15 K, 1 atm	19.9	15.8
	Ethanol	CH ₃ CH ₂ OH	789 at 293.15 K, 1 atm	26.8	21.1
	Ammonia	NH ₃	681 at 239.75 K, 1 atm	18.6	12.7
	Liquefied Petroleum Gas (LPG)	C ₃ H ₈ /C ₄ H ₁₀	550 at 293.15 K, 8 atm	46.0	25.3
Cryogenic	Biodiesel	C ₁₂ –C ₂₂ FAMEs	880 at 288.15 K, 1 atm	37.8	33.3
	Liquid Methane (LM)	CH ₄	422 at 111.65 K, 1 atm	50.0	21.1
	Liquefied Natural Gas (LNG)	CH ₄ /C ₂ H ₆ /C ₃ H ₈ /C ₄ H ₁₀	450 at 111.15 K, 1 atm	48.6	21.9
	Liquid Hydrogen (LH ₂)	H ₂	71 at 20.35 K, 1 atm	120.0	8.5

Well-to-Tank: Energy and Emissions

The specific energy metric from Table 1 was primarily used in this study for the selection of alternative fuels, including LH₂, LPG, and LNG. While LH₂ is associated with the highest overall specific energy, the liquid hydrocarbon fuels, LPG and LNG, display a higher specific energy than ammonia or alcohol-based counterparts. The alternative fuels are compared with the baseline fuel, Jet-A, from Table 1. As a first step in the analysis of an alternative fuel, the well-to-tank energy and emissions are evaluated, encompassing the critical production stage of the fuel. While a detailed well-to-tank analysis doesn't form the focus of the present article, a summary of the methodology and the main results have been included for completeness. The schematic in Figure 1 highlights the well-to-tank system processes and boundary. The primary resources in the envisioned system include energy, H₂O, and CO₂. The energy is assumed to be supplied from a fully renewable electricity grid. A PEM electrolyzer is used to produce H₂ from energy and H₂O assuming a mean electrolysis efficiency of 80% from the literature [20, 21]. The H₂ from the electrolyzer combines with

CO_2 in a CO_2 hydrogenation reactor to produce a series of hydrocarbons, comprising of both fuel and by-products. The output of the CO_2 hydrogenation reactor also includes a small quantity of unburnt H_2 , UH_2 , and CO_2 , UCO_2 , resulting from an expected conversion of 90% [22]. A CO_2 separator is utilized to extract UCO_2 for recycling, leading to a reduction in the overall CO_2 demand. The remaining output after the removal of unburnt CO_2 is supplied to an H_2 separator and a fractional distillation unit for the separation of the mixture into UH_2 , fuel, and by-products. An empirical method is used for the detailed modeling of the CO_2 hydrogenation process. In this method, the output hydrocarbons are defined using empirical product distributions based on the path of hydrogenation, including the Fischer-Tropsch and methanol-intermediate hydrogenation routes. For instance, the ASF product distribution [23] is used in the case of Fischer-Tropsch hydrogenation. The results presented in this section correspond to the hydrogenation route associated with the lowest energy demand. Finally, the combustion of by-products from CO_2 hydrogenation is assumed to power such sub-processes as the heating and compression of H_2 and CO_2 for CO_2 hydrogenation, separation of fuel and by-products through fractional distillation, fuel liquefaction, etc.

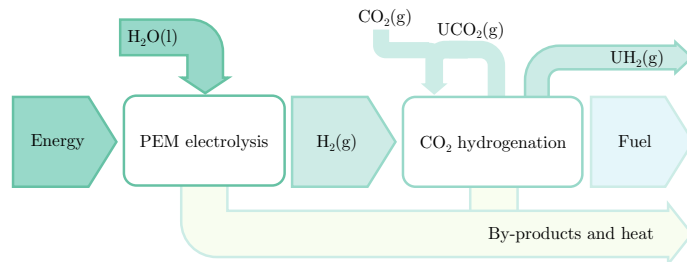


Fig. 1 Well-to-Tank system boundary and major processes.

Figure 2 shows the flow of energy in terms of percentage across the entire well-to-tank system for Jet-A, LPG, and LNG. The corresponding product distributions are presented in Figure 3 in terms of the mole fraction of hydrocarbons from C_1 to C_{20} . Returning to Figure 2, the percentage basis enables direct reading of the production efficiency, defined as the ratio of the fuel energy content to the energy input to the system. It should be noted that the production efficiency for LH_2 is merely the PEM electrolyzer efficiency of 80% used in this study. The other fuels are associated with comparable efficiencies between 49% and 53%. As a note of validation of the current well-to-tank analysis, the Jet-A efficiency of 49% aligns favorably with the 57% and 48% efficiencies reported for similar hydrocarbon fuels in the literature [24, 25].

The input CO_2 , referred to as feedstock CO_2 , and GHG emissions from the burning of hydrogenation by-products are presented in Table 2 using a per MJ of fuel basis. The lower heating value of each fuel is utilized for the per MJ of fuel basis calculation. The GHG emissions in this section and the rest of the document are presented in terms of the CO_2 equivalent metric, CO_2e , using a 100-year global warming potential, GWP₁₀₀. Unlike the well-to-tank input energy demand, which is comparable across the board in Figure 2, the feedstock CO_2 demand for LPG and LNG are approximately 13% and 22% lower than the corresponding demand for Jet-A. The reduced feedstock CO_2 demand stems from the lower Carbon number to heating value ratio for LPG and LNG due to the dominance of C_{1-4} hydrocarbons in the composition of these fuels in comparison with Jet-A, which mainly comprises of C_{8+} hydrocarbons. Furthermore, due to the particular prominence of C_1 hydrocarbon in the LNG composition, this fuel is associated with the lowest Carbon number to heating value ratio and consequently, the lowest overall feedstock CO_2 demand from amongst the non- LH_2 fuels. Prior to the next discussion, it should be noted that the results from Table 2, including the energy demand presented in terms of the same per MJ of fuel basis, will be recalled later in this paper for a comprehensive evaluation of the alternative fuels.

Table 2 Summary of the Well-to-Tank results.

Fuel	Energy [MJ/MJ _{fuel}]	Feedstock [gCO ₂ /MJ _{fuel}]	GHG Emissions [gCO ₂ e/MJ _{fuel}]
Jet-A	2.024	73.588	7.979
LPG	1.985	63.933	6.070
LNG	1.919	57.139	5.942
LH ₂	1.250	0	0



Fig. 2 Sankey diagrams showing the flow of energy across the well-to-tank system.

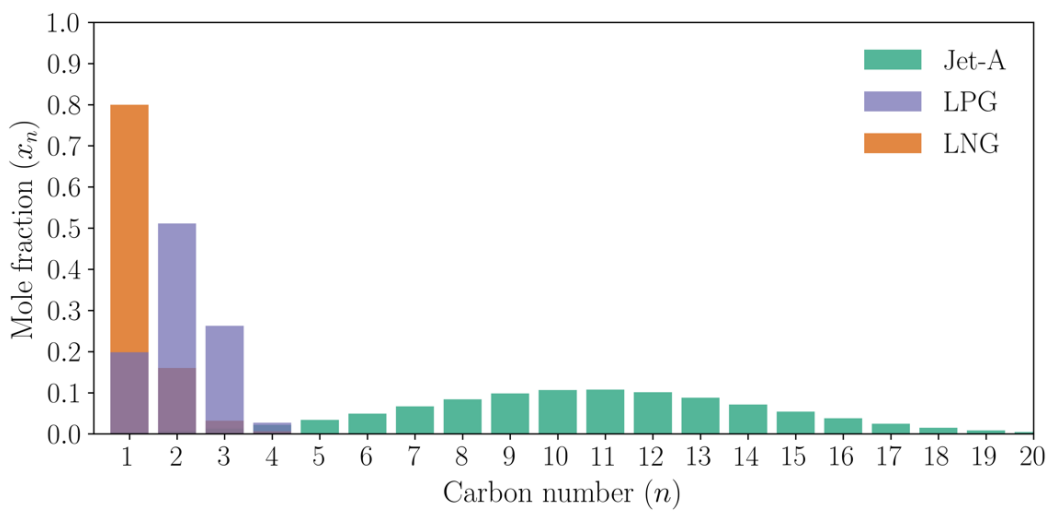


Fig. 3 CO₂ hydrogenation product distributions.

III. Computational Modeling

This chapter outlines the modeling framework and simulation architecture developed for the study. Section III.A begins with an overview of the RCAIDE environment, emphasizing its modular structure and integrated workflow for analyzing alternative energy carriers. Section III.B introduces five representative aircraft models selected to reflect major categories within U.S. domestic operations, detailing their key characteristics. It also describes the flight parameters used to define representative mission profiles for each aircraft class. Section III.C presents the formulation of power and propulsion system models, which serve as the core of both mission performance and emissions analysis. This section includes a validation of the baseline turbofan engine architecture. Section III.D addresses aircraft weight and performance estimation across relevant flight conditions, along with validation of payload–range charts and operational empty weight (OEW) for each aircraft model. Section III.E introduces a high-fidelity Chemical Reactor Network (CRN) model representing a Rich-Burn, Quick-Mix, Lean-Burn (RQL) combustor, developed to predict direct emissions from various alternative fuels under different engine operating conditions. This section also presents validation of the CRN model against benchmark LTO data for key emission species: CO₂, H₂O, NO_x, and CO. Finally, Section III.F outlines the parameterization of fuel properties used to model Liquid Hydrogen (LH₂), Liquefied Petroleum Gas (LPG), and Liquefied Natural Gas (LNG) within the simulation framework.

A. Simulation Environment

The Research Community Aerospace Interdisciplinary Design Environment (RCAIDE), developed by the Laboratory for Electric Aircraft Design and Sustainability (LEADS) at the University of Illinois Urbana-Champaign, is an open-source, Python-based computational framework for the conceptual design, analysis, and optimization of aerospace systems [26]. Designed to support a wide range of vehicle architectures, from conventional tube-and-wing aircraft to unconventional vertical takeoff and landing configurations, RCAIDE provides a cost-effective and flexible alternative to high-fidelity simulation environments, enabling rapid iteration and early-phase trade studies with reduced computational overhead [27]. The modular structure of the framework supports sequential and integrated simulations across various disciplines, including aerodynamics, propulsion, performance, and emissions. Figure 4 illustrates the overarching simulation logic and workflow architecture of the software.

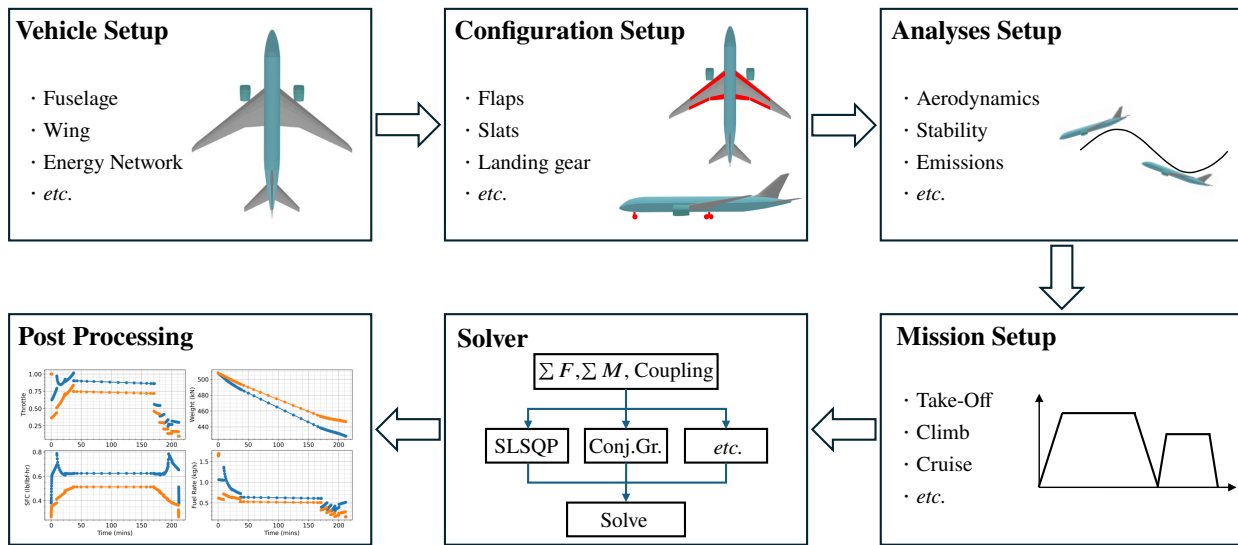


Fig. 4 RCAIDE modeling and simulation workflow.

The process begins with the **Vehicle Setup**, where core parameters such as geometry, propulsion architecture, and mass properties are initialized. This is followed by the **Configuration Setup**, which defines various aircraft configurations (e.g., Take-Off with flaps deflected, cruise, descent with spoilers deployed, and landing gear down) used throughout the mission profile. Next, in the **Analyses Setup**, users can configure the required analysis. A summary of the relative methods and approaches used for this work is shown in Table 3. The **Mission Setup** outlines the flight

kinematics within each flight segment and the relative operating conditions, such as altitude and heading, and synthesizes inputs from the previous setup stages. These components feed into the **Solver** module, which executes the simulation and computes performance metrics across the mission timeline. Finally, the **Post Processing** block visualizes key outputs such as fuel consumption, altitude profiles, and energy use.

Table 3 RCAIDE analyses employed in this study.

Analysis	Method	Approach	Reference
Aerodynamics	Vortex Lattice Method	Surrogate	[28]
Stability	Vortex Lattice Method	Surrogate	[28]
Atmosphere	Standard Atmosphere	US Standard 1976	[29]
Emissions	Emission Index	CRN	[12, 30, 31]
Navigation	Geodesic Distance	WGS-84	[32]
Geometry	Geometry	Airfoil, Planform	[33, 34]
Weights	Conventional	CG, MOI, FLOPS	[35]
Propulsion	Polytropic	Refer to Section III.C	[30, 36]

B. Aircraft Models and Flight Operations

To ensure a representative selection of aircraft for this study, a comprehensive analysis was conducted using operational records from the 2019 U.S. Bureau of Transportation Statistics (BTS) [37]. This dataset includes extensive details on flight routes, passenger volumes, flight frequencies, fuel consumption, and other operational parameters across the U.S. domestic air transportation system. However, a direct mapping between aircraft tail numbers and flight-level operations was not readily available, as tail numbers are stored separately from route-level statistics. While a complete cross-referencing using the FAA registry could have been automated, it was deemed impractical given the volume of data and the limited marginal benefit. To address this limitation, a rigorous estimation methodology was developed, wherein average aircraft seating capacity was inferred from passenger counts and flight frequencies at the route level. This allowed for a reasonable approximation of the types of aircraft most frequently deployed on various domestic missions. Figure 5 illustrates the aggregated U.S. domestic air routes for each aircraft capacity. Different aircraft classes tend to serve distinct regions and routes within the domestic network. Figure 6a presents the range-based distribution of annual U.S. domestic passengers by aircraft class. Notably, aircraft with an estimated maximum capacity of 189 passengers account for the highest share of annual passengers, particularly on routes spanning up to approximately 3,000 nautical miles. This is further emphasized in Figure 6b, which compares total passenger volumes across all capacity classes.

Based on this approach, five aircraft were selected to span the full spectrum of typical U.S. domestic operations: the de Havilland Canada DHC-6-300 [38], ATR 72-600 [39], Embraer E190 STD [40], Boeing B737-800, and Boeing B777-200ER [41]. These aircraft capture a wide range of mission profiles, from short-haul regional commuter flights to long-haul, high-capacity routes. To validate the soundness of this selection, multiple randomly chosen flights were manually checked against real-world data available via Google Flights. This cross-verification confirmed the alignment between modeled aircraft types and those actually deployed in service by major U.S. carriers. Key performance and design characteristics for each aircraft are summarized in Table 4.

The simulation methodology employed in this study requires the definition of a representative mission flight profile for each aircraft type, as discussed in Section III.A. To maintain consistency across the different aircraft classes, a standard set of flight segments was used, comprising: Takeoff Ground Run, Takeoff Climb, Initial Climb, Climb to Cruise, Cruise, Descent from Cruise, Final Descent, Approach, Level Off, and Landing Roll. Table 5 details the representative flight profile adopted for the Boeing 737-800, specifying key parameters such as altitude and airspeed for each flight segment. Analogous mission profiles were developed for the DHC-6-300, ATR 72-600, Embraer 190 STD, and Boeing 777-200ER. These profiles, adapted to reflect the performance characteristics of each aircraft, are provided in Appendix A. Once the flight missions are simulated, the emission indices corresponding to each flight segment are retrieved. By multiplying the fuel consumed in each segment by the respective emission index, the total emissions of each species can be computed. To compare results across different species, the emission values are normalized by their associated 100 year Global Warming Potential (GWP₁₀₀). The GWP₁₀₀ values adopted in this study are the same presented in Section II, based on [5], while emissions are expressed in terms of gCO₂e/RPK.

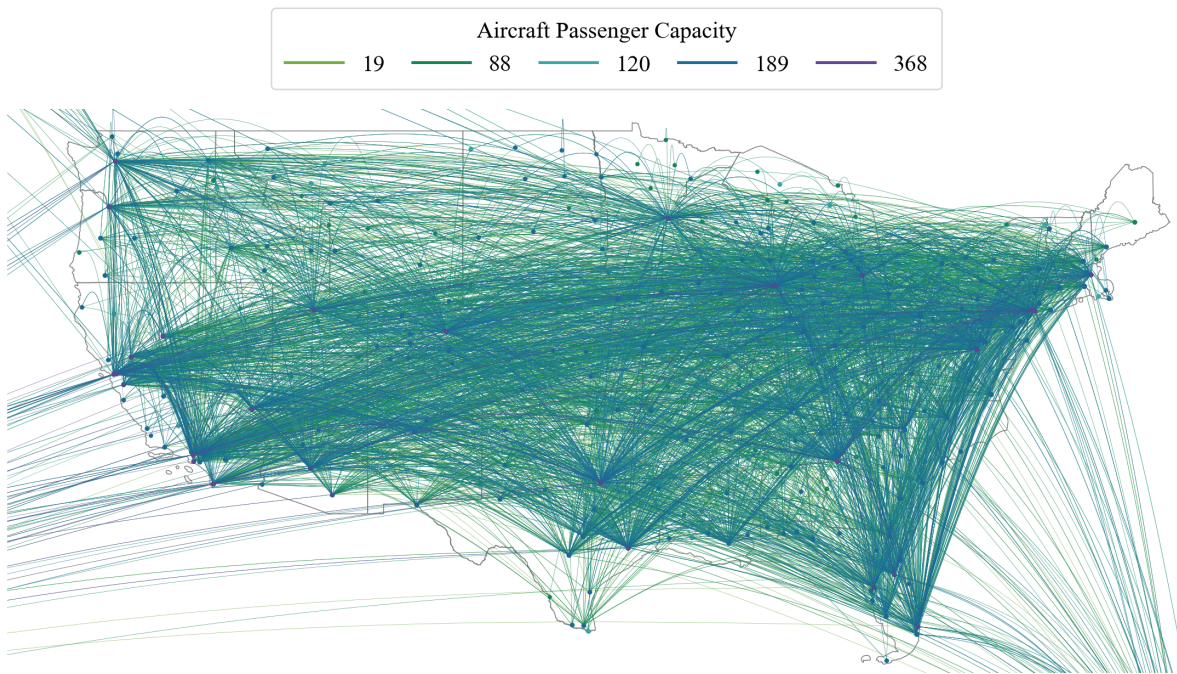


Fig. 5 Domestic aviation routes aggregated by five aircraft capacity classifications. Flights to Alaska and other island states of the United States are not shown but are included in calculations.

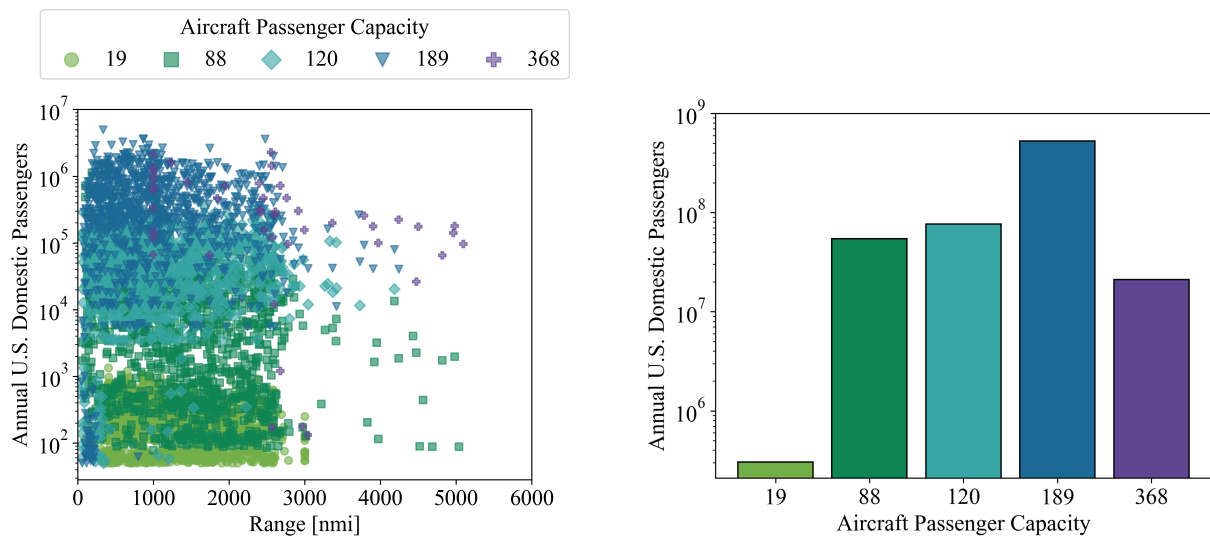


Fig. 6 Passenger distribution across range (left) and aircraft class (right) for U.S. domestic operations.

Table 4 Specifications for the selected aircraft in the study

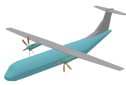
	DHC-6-300	ATR 72-600	E190 STD	B737-800	B777-200er
					
Class	Commuter	Regional	Short haul	Medium haul	Long haul
Propulsion	Turboprop	Turboprop	Turbofan	Turbofan	Turbofan
MTOW [lbs / kg]	14,021 / 6,360	50,265 / 22,800	114,199 / 51,800	174,200 / 79,016	634,500 / 287,804
OEW [lbs / kg]	8,180 / 3,710	28,682 / 13,010	61,370 / 27,837	91,300 / 41,413	299,500 / 135,850
Payload [lbs / kg]	2,500 / 1,135	16,645 / 7,550	28,800 / 13,063	52,800 / 23,950	120,000 / 54,431
Fuel [US gal / L]	378 / 1,466	1,645 / 6,228	4,268 / 16,156	6,875 / 26,022	45,220 / 171,176
Range [nmi / km]	799 / 1,480	758 / 1,404	2,450 / 4,537	2,935 / 5,436	6,500 / 12,038
S_{ref} [ft² / m²]	420 / 39	665 / 61	996 / 93	1,341 / 125	4,605 / 427.8

Table 5 Flight profile segments for the B737-800 reference mission.

Flight Segment	Altitude [ft]	Airspeed [knots]	Vertical Rate / Note
Takeoff Ground Run	0	0–167	Friction Coef: 0.03
Takeoff Climb	0–35	167–175	250 fpm
Initial Climb	35–1,000	200	1,800 fpm
Climb to Cruise	1,000–40,000	200–300	1,700 fpm
Cruise	40,000	450	Distance: 5000 km
Descent from Cruise	40,000–10,000	380	-1,850 fpm
Final Descent	10,000–2,000	225	-650 fpm
Approach	2,000–50	175	-600 fpm
Level Off	50–0	160	-300 fpm
Landing Roll	0	160–10	Friction Coef: 0.4

C. Power and Propulsion

At the core of the simulation framework is the powertrain network, a system-level representation composed of interconnected elements that model the physical and functional subsystems of the propulsion architecture. These components are categorized into five primary functional groups: Converters, Distributors, Modulators, Propulsors, and Sources. Converters are responsible for transforming energy from one form to another or modifying it within the same domain to yield a desired output. This category includes the key thermodynamic elements of the propulsion cycle, namely the fan, compressor, combustor, turbine, and nozzle, which together define the operating characteristics of the engine. Each converter module corresponds to a distinct physical process (e.g., compression, combustion, expansion) and is modeled using a polytropic-based formulation, as detailed by Cantwell [30]. The modular architecture implemented in RCAIDE ensures that each component is treated as a Subsystem of the powertrain System of Interest (SoI), enabling independent characterization and integration within the powertrain network. The output of the powertrain SoI directly influences aircraft-level performance metrics, with the complete aircraft treated as a System of Systems (SoS). This hierarchical modeling approach facilitates the integrated assessment of aircraft performance, direct emissions, and operational characteristics across multiple aircraft configurations and alternative energy carriers. An illustration of this hierarchical structure is shown in Figure 7. The diagram presents a representative narrow-body aircraft SoS, its associated turbofan propulsion SoI, and the embedded Rich-Burn, Quick-Mix, Lean-Burn (RQL) combustor subsystem.

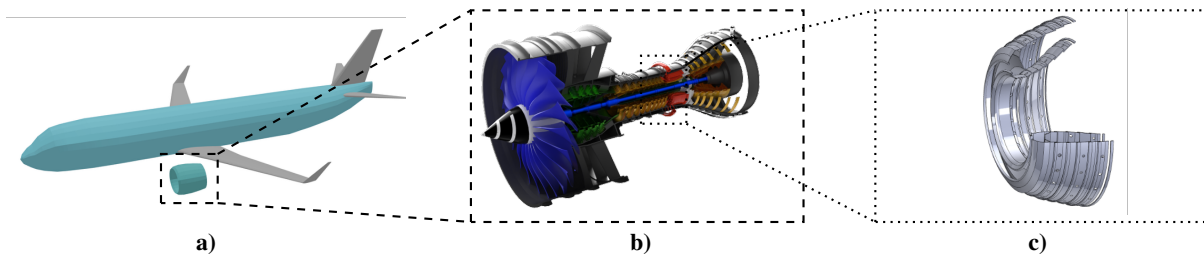


Fig. 7 Diagram of hierarchical powertrain system architecture: a) Aircraft System of Systems (SoS), b) Turbofan Engine System of Interest (SoI), c) RQL Burner Subsystem.

In addition to Converters, the remaining functional elements play essential roles in the simulation architecture. Distributors manage the allocation of mass, energy, or power across subsystems, enabling coordinated flow within the network. Modulators regulate power flow to ensure stable and controlled system behavior under varying operating conditions. Propulsors serve as a specialized subset of converters that work in concert to generate thrust by transforming thermodynamic energy into mechanical force. Sources represent energy storage components, such as fuel tanks or batteries, and act as the origin of energy flow within the system.

Table 6 provides a comparative evaluation of the GE90 turbofan engine model implemented in RCAIDE. The benchmarking includes reference data from the Gas Turbine Simulation Program (GSP) [42], a high-fidelity gas turbine modeling tool incorporating performance maps and off-design capability, as well as a previously validated analytical model developed by Proesmans and Vos [36]. The latter utilized a simplified thermodynamic method for both design and off-design analysis and was verified against GSP results and performance trends from GE90 engine data compiled by Nicolai and Carichner [43].

Table 6 Comparison of GE90 engine performance parameters from GSP, Proesmans & Vos [36], and the RCAIDE model implementation

Parameter [Unit]	GSP	Proesmans & Vos [36]	RCAIDE
Compressor Exit Temperature [K]	771	772 (+0.09%)	786.74 (+2.04%)
Compressor Exit Pressure [MPa]	1.42	1.42 (+0.04%)	1.43 (+1.19%)
Turbine Inlet Temperature [K]	1430	1430 (0.00%)	1430 (0.00%)
Turbine Inlet Pressure [MPa]	1.35	1.35 (+0.04%)	1.35 (0.00%)
Fuel Mass Flow Rate [kg/s]	1.14	1.16 (+1.37%)	1.18 (+3.50%)
TSFC [mg/(N s)]	14.6	14.9 (+1.75%)	15.21 (+4.17%)

The RCAIDE implementation shows strong agreement with established GE90 engine performance benchmarks, demonstrating its validity for system-level propulsion analysis. The model accurately reproduces turbine inlet conditions and exhibits only minor deviations in compressor exit parameters. Specifically, the compressor exit temperature predicted by RCAIDE is within 2.04% of GSP results. Similarly, the predicted compressor exit pressure shows a marginal deviation of +1.19%. The fuel mass flow rate shows a small overestimation of +3.50%, while TSFC is predicted at 15.21 mg/(N·s), a 4.17% increase relative to the GSP baseline. These discrepancies are consistent with previous findings by Proesmans and Vos [36], who highlight that differences between simplified models and high-fidelity tools such as GSP are primarily due to assumptions related to specific heat models and the absence of performance maps.

D. Aircraft Performance Validation

For each of the five selected aircraft, the payload–range characteristics are validated against reference data available in the literature, as illustrated in Figure 8a. Additionally, the Operating Empty Weight (OEW) for each aircraft is estimated based on available specifications and weight breakdown methodologies (see Figure 8b). These are compared to the listed manufacturer values provided in Table 7 below.

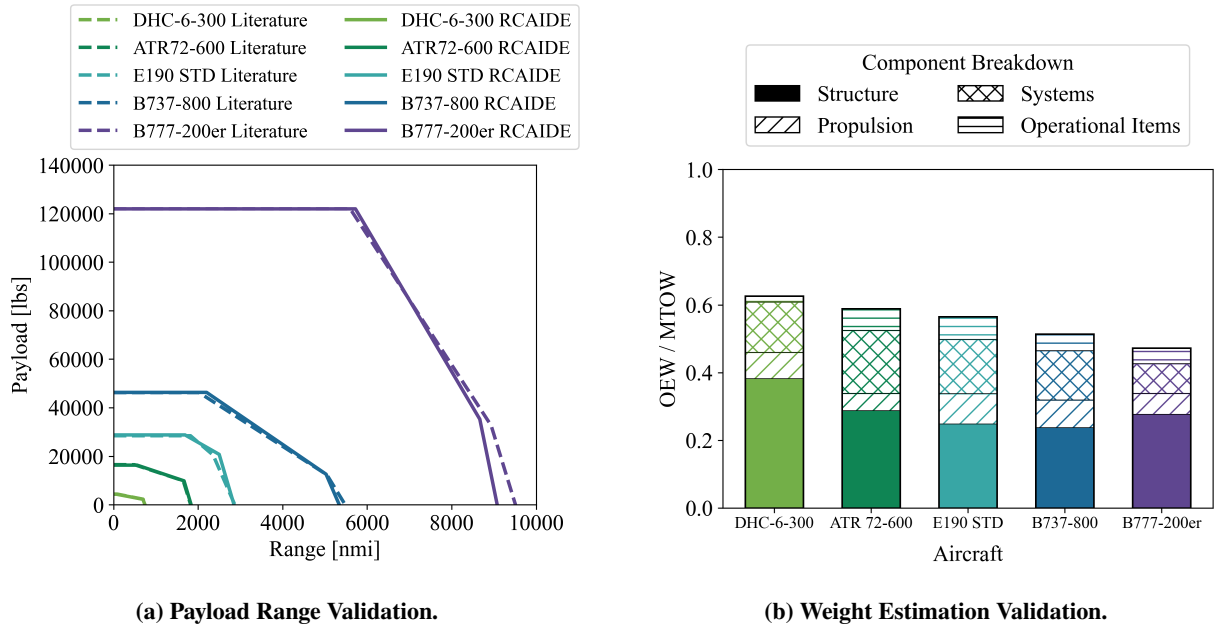


Fig. 8 Payload range and weight breakdown diagrams for the different aircraft classes.

Table 7 Operating Empty Weight (OEW) validation against literature.

Source	DHC-6-300 [lbs]	ATR 72-600 [lbs]	E190 STD [lbs]	B737-800 [lbs]	B777-200er [lbs]
Literature	7,415	29,983	61,370	91,300	299,550
RCAIDE	7,907 (+6.64%)	29,846 (-0.46%)	64,575 (+5.22%)	89,582 (-1.88%)	309,901 (+3.46%)

E. Direct Emissions

Central to emissions production is the operation of the gas turbine engine, specifically the combustor, where the conversion from chemical to kinetic energy happens. In order to fully understand the production mechanisms of GHGs, the combustion process has to be investigated, involving rapid fuel oxidation and the generation of significant heat. This process typically involves air as the oxidizer and either liquid or gaseous fuels and is inherently complex, unsteady, and turbulent, governed by non-linear partial differential equations.

Different approaches can be employed to model aircraft engine emissions effectively. Lower-fidelity, correlation-based models offer a computationally inexpensive solution for preliminary assessments. An example of such a model is provided in Equation 1.

$$EI_{NO_x} = \frac{1.5 \times 10^{15} (\tau - 0.5\tau_{evap})^{0.5} \exp\left(\frac{-71,100}{T_{st}}\right)}{P_3^{0.05} \left(\frac{\Delta P_3}{P_3}\right)^{0.5}} \quad (1)$$

Other methods, such as the P3T3 method, require proprietary input parameters. In contrast, fuel flow-based models like BFFM2 and the DLR method offer greater flexibility. However, these methods have notable limitations. Specifically, they cannot account for fuel composition effects, and their polynomial curve fits cannot be confidently extrapolated to engine conditions where T_3 and/or P_3 lie outside the range of the original calibration data. Furthermore, they rely on reference datasets specific to particular engine-combustor configurations. These models are typically validated against extensive datasets for conventional fuels and serve as useful tools for initial emissions estimations. Nonetheless, their dependence on specific reference data constrains their applicability. They often fail to capture the influence of different combustor designs or variations in engine operating conditions. Additionally, limited data is available

regarding emissions from unconventional fuels in aircraft applications, further restricting the predictive capability of these approaches.

In contrast, higher-fidelity models, such as three-dimensional Large Eddy Simulations (3D LES), provide more accurate estimations of combustion emissions by explicitly modeling the combustion process within the engine. These methods offer the capability to assess the influence of various combustor designs, operating conditions, and fuel types. Despite their accuracy and flexibility, LES models are associated with substantial computational costs, making them impractical for rapidly quantifying the effects of different fuel compositions and combustor configurations across a wide design space. Nevertheless, for the preliminary design of unconventional aircraft systems, higher-fidelity models remain a key enabler, offering the resolution necessary to evaluate the impacts of alternative energy carriers on aircraft emissions and operations.

As a consequence, simplified zero-dimensional (0D) and one-dimensional (1D) models based on chemical reactor networks (CRNs) have been developed. A chemical reactor network models the combustor as a collection of interconnected reactors, each representing specific zones within the combustor. The configuration, placement, and type of these reactors are informed by experimental techniques, such as Particle Image Velocimetry (PIV), or by results from Computational Fluid Dynamics (CFD) simulations. While CFD enables detailed modeling of fluid flow, heat transfer, and combustion processes, making it well-suited for analyzing complex geometries and flow characteristics, it is typically resource-intensive in terms of time and computational requirements. Moreover, the use of simplified chemistry assumptions within CFD can introduce potential inaccuracies. In contrast, the CRN approach emphasizes chemical reactions and species distribution by representing the flow field as a network of interconnected reactors. This method reduces computational time and simplifies flow and turbulence modeling, at the expense of neglecting the direct coupling between turbulence and chemical reactions [44].

Nevertheless, previous studies, such as those by Allaire [45] and Chowdhury [46], have demonstrated the capabilities of CRNs in modeling combustors and predicting aircraft emissions. Specific kinetic mechanisms can describe different fuel types, defining the unique chemical species and reactions involved in the combustion processes. Kinetic mechanisms are, therefore, a key element in analyzing specific fuel compositions and combustion conditions and their influence on emissions, guiding the design of combustors for improved performance and an overall better environmental impact.

Shown in Fig. 9, the general schematic of a RQL burner and the building blocks of the combustor CRN: Perfectly Stirred Reactors (PSRs) and Plug Flow Reactors (PFRs). The PSR models steady, one-dimensional flow through a reactor, assuming ideal gas behavior. It represents an idealized reactor with complete, instantaneous mixing within a defined control volume. The primary assumption for this reactor is that mixing is uniform and immediate, resulting in no temperature or species concentration gradient. This model is, therefore, suitable for scenarios where turbulent eddy motion timescales are shorter than chemical reaction timescales. In these cases, mixing occurs so quickly that the chemistry becomes a rate-determining factor, allowing PSRs to accurately model combustion kinetics. In a PFR, reactant concentrations vary along the reactor's axial direction while remaining uniform radially, so there are no concentration gradients perpendicular to the flow. The model assumes complete radial mixing, with no mixing in the axial direction, creating a "plug" of reactants that moves through the reactor. This setup is particularly effective for analyzing reactions where chemical kinetics and temperature changes occur progressively along the length of the reactor.

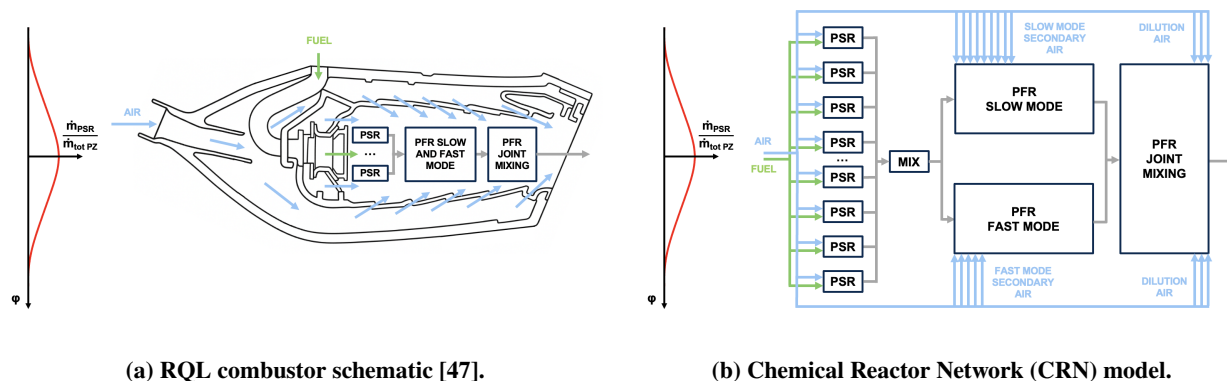


Fig. 9 RQL burner architecture and RCAIDE modeling using a Chemical Reactor Network approach.

The assembly of different PSRs and PFRs allows the creation of complex networks called "Chemical Reactor Networks." In this paper, the combustor model has been implemented within RCAIDE. By employing Cantera [16], an open-source toolkit for chemical kinetics, thermodynamics, and transport processes, the framework supports detailed reaction mechanism simulations within each reactor. Cantera facilitates the calculation of species concentrations and reaction rates crucial for emissions predictions, enabling the capture of the intricacies of chemical kinetics involved in combustion processes. This integration of RCAIDE with CRN models enhances the accuracy of emissions estimation under various operating conditions, combustor designs, and alternative energy carriers while maintaining computational efficiency [12].

Combustor architecture is typically composed of two main zones: the Primary and Secondary Zone. The Primary Zone is responsible for anchoring the flame and ensuring near-complete combustion of the fuel-air mixture. This zone is characterized by high turbulence and recirculation, which enhances mixing and provides for a stable flame. The Secondary Zone follows, where combustion is completed and dissociation losses (caused by bonds breaking at high temperatures in the Primary Zone) are managed. To start, air instantaneously added to cool the fuel-air mixture that is hot from the previous zone. Then, secondary air is gradually introduced to maintain optimal temperatures without significantly affecting combustion. Finally, dilution air is added which reduces the gas temperature to levels suitable for turbine entry and ensures temperature uniformity across the combustor exit plane.

To reduce nitrogen oxide (NO_x) emissions while maintaining performance across a broad operating envelope, many modern aeroengine combustors adopt the Rich-Burn, Quick-Mix, Lean-Burn (RQL) strategy. This configuration initiates combustion in a fuel-rich primary zone, typically modeled as a network of perfectly stirred reactors (PSRs), where lower flame temperatures suppress NO_x formation. Rapid quenching follows via the injection of secondary air, transitioning the flow into a lean-burn secondary zone designed to complete combustion efficiently while minimizing thermal dissociation and associated losses. This structured approach enables precise control of temperature and mixing, aligning with the stringent emissions and operability requirements of aerospace propulsion systems.

Originally introduced in the 1980s as a method for NO_x mitigation, the RQL concept gained traction through NASA-led research in the 1990s targeting next-generation low-emission engines. Today, RQL technology is central to commercial aeroengine combustors, such as Pratt & Whitney's TALON (Technology for Advanced Low NO_x) system. Compared to lean-premixed alternatives, RQL configurations offer superior flame stability and robustness throughout the engine duty cycle, making them particularly well-suited for aviation applications.

The CRN model captures the unsteady behavior of mass, chemical species, and energy, while accounting for the vaporization of liquid fuel prior to combustion. The transient behavior of the Primary Zone is governed by conservation laws for mass, species, and energy. These equations are solved simultaneously to capture the coupled thermochemical dynamics of the combustion process and are critical for predicting combustion behavior, fuel efficiency, and emissions [47].

The total mass inside the reactor evolves according to the following expression:

$$\frac{dm}{dt} = \dot{m}_{\text{in}} - \dot{m}_{\text{out}} \quad (2)$$

The outlet mass flow rate \dot{m}_{out} is computed by introducing a pressure-dependent correction that reflects the imbalance between the reactor pressure P and a reference inlet pressure P_0 :

$$\dot{m}_{\text{out}} = \dot{m}_{\text{in}} + K_v(P - P_0) \quad (3)$$

where, $K_v = 0.001 \text{ kg}/(\text{s} \cdot \text{Pa})$ serves as a tuning coefficient linking pressure deviation to excess outlet mass flow. For each species k , the mass fraction Y_k inside the reactor is governed by:

$$\frac{dY_k}{dt} = \frac{\dot{\omega}_k W_k}{\rho_{\text{gas}}} + \frac{\dot{m}_{\text{in}}(Y_{k,\text{in}} - Y_k)}{m} \quad (4)$$

where $\dot{\omega}_k$ is the molar production rate of species k [$\text{kmol}/(\text{m}^3 \cdot \text{s})$], W_k is its molecular weight [kg/kmol], ρ_{gas} is the gas density [kg/m^3], and $Y_{k,\text{in}}$ is the inlet mass fraction of species k . The subscript "in" denotes properties of the inflow stream. The temperature evolution within the Primary Zone is captured by the energy equation for an ideal gas reactor at constant pressure:

$$\frac{dT}{dt} = \frac{1}{mc_p} \left[\dot{m}_{\text{in}} \left(h_{\text{in}} - \sum_{k=1}^K h_k Y_{k,\text{in}} \right) - \sum_{k=1}^K h_k \dot{m}_{k,\text{gen}} \right] \quad (5)$$

In this formulation, m is the total mass of the reactor contents, c_p is the specific heat at constant pressure [J/(kg · K)], K is the number of chemical species, h_k is the specific enthalpy of species k , and $\dot{m}_{k,\text{gen}}$ is the mass generation rate of species k , computed as:

$$\dot{m}_{k,\text{gen}} = V_{\text{PZ}} \dot{\omega}_k W_k \quad (6)$$

where, V_{PZ} denotes the volume of the Primary Zone. Since the fuel is injected in liquid form at standard atmospheric conditions ($T = 298.15$ K, $P = 101,325$ Pa), an energy correction is required to account for its vaporization prior to combustion. This correction modifies the enthalpy of the fuel-air mixture at station 3 (T_3 , P_3) as follows:

$$h_{\text{mix}} = \frac{1}{\dot{m}_{\text{mix}}} [\dot{m}_{\text{air}} h_{\text{air}, P_3 T_3} + \dot{m}_{\text{fuel}} h_{\text{fuel}, P_3 T_3} - \dot{m}_{\text{fuel}}(L + \Delta h)] \quad (7)$$

In this equation, $h_{\text{air}, P_3 T_3}$ and $h_{\text{fuel}, P_3 T_3}$ are the specific enthalpies of air and fuel at the combustor inlet conditions. L is the latent heat of vaporization [J/kg], and Δh accounts for the sensible enthalpy increase of the fuel from standard conditions up to T_3 , P_3 .

To capture the spatial non-uniformity in fuel-air mixing within the Primary Zone (PZ), the equivalence ratio (ϕ) is distributed among the perfectly stirred reactors (PSRs) using a Gaussian profile. This approach accounts for local variations in fuel concentration that influence combustion completeness and pollutant formation. The PZ is characterized by intense recirculation and turbulence, which promote effective mixing and flame stabilization. Despite the high flame temperatures, NO_x formation remains relatively low in this zone due to localized oxygen depletion. The N_{PZ} PSRs are each assigned a specific equivalence ratio, ϕ_i , sampled from a normal distribution centered around a mean value $\bar{\phi}$ with standard deviation $\sigma_{\bar{\phi}}$, which quantifies the degree of non-uniformity in the PZ. In the limiting case of perfect mixing, $\sigma_{\bar{\phi}} = 0$, and the distribution collapses to a delta function. The fraction of total mass flow allocated to each reactor is given by:

$$f(\phi_i) = \frac{1}{\sigma_{\bar{\phi}} \sqrt{2\pi}} \exp\left(-\frac{(\phi_i - \bar{\phi})^2}{2\sigma_{\bar{\phi}}^2}\right) \Delta\phi \quad (8)$$

where, $\Delta\phi$ represents the bin width, which becomes narrower as the number of PSRs increases. The standard deviation $\sigma_{\bar{\phi}}$ is computed using a dimensionless mixing indicator S_{PZ} , defined as:

$$S_{\text{PZ}} = \frac{\sigma_{\bar{\phi}}}{\bar{\phi}} \quad (9)$$

The mean equivalence ratio $\bar{\phi}_j$, associated with engine thrust level j , is determined from the fuel and air mass flow rates and the stoichiometric fuel-to-air ratio FAR_{st}:

$$\bar{\phi}_j = \frac{\dot{m}_{\text{fuel},j}}{f_{\text{air}, \text{PZ}} \dot{m}_{\text{air},j} \text{FAR}_{\text{st}}} \quad (10)$$

Larger values of S_{PZ} correspond to greater inhomogeneity in the fuel-air distribution. In this model, S_{PZ} is assumed to depend solely on combustor design parameters, reflecting the influence of fuel injection and airflow configuration. Potential dependencies on operating conditions or equivalence ratio are not considered due to limited available data. At maximum thrust, the primary zone design equivalence ratio $\phi_{\text{PZ},\text{des}}$ is used to determine the fraction of total air directed into the PZ, denoted as $f_{\text{air}, \text{PZ}}$. This is computed using:

$$f_{\text{air}, \text{PZ}} = \frac{\dot{m}_{\text{fuel,takeoff}}}{\phi_{\text{PZ},\text{des}} \dot{m}_{\text{air,takeoff}} \text{FAR}_{\text{st}}} \quad (11)$$

where $\dot{m}_{\text{fuel,takeoff}}$ and $\dot{m}_{\text{air,takeoff}}$ are the fuel and air mass flow rates at takeoff, respectively. Lastly, the residence time in reactor i is given by:

$$t_{\text{res},i} = \frac{\rho_i V_{\text{PZ},i}}{\dot{m}_{\text{fuel},i} + \dot{m}_{\text{air},i}} \quad (12)$$

This expression relates the local gas density ρ_i , reactor volume $V_{\text{PZ},i}$, and the total incoming mass flow to the time available for chemical reactions to occur within each PSR.

In the Secondary Zone of the combustor, the main objective is to complete the combustion process and reduce the temperature of the gas mixture. If secondary air is gradually introduced into the combustion products from the primary zone, both the temperature and oxygen concentration increase progressively, which significantly promotes NO_x formation. Conversely, if the additional air is mixed rapidly and uniformly, the risk of further NO_x production can be mitigated. Thus, the role of the quick-mix section is to ensure fast and homogeneous mixing of secondary air, minimizing temperature overshoots and emissions.

Although the majority of the fuel is burned in the primary zone, residual species such as CO, H₂, and unburned hydrocarbons remain. The secondary zone introduces additional air to oxidize these species. Despite the resulting lean mixture, the lower temperature relative to the primary zone helps limit further NO_x formation.

The conservation of mass in the Secondary Zone is modeled as:

$$\frac{d\dot{m}_{\text{gas}}}{dz} = \beta_{\text{air,in}} \quad (13)$$

where $\beta_{\text{air,in}}$ denotes the axial rate of air injection per unit length [kg/(s·m)] along the combustor. Species transport is formulated using a plug-flow reactor (PFR) model, modified to include secondary air mixing. Starting from the general species conservation equation:

$$\rho u \frac{dY_k}{dz} + Y_k P' \sum_{k=1}^K \dot{s}_k W_k = \dot{\omega}_k W_k + P' \dot{s}_k W_k \quad (14)$$

where u is the axial gas velocity [m/s], \dot{s}_k is the surface molar production rate of species k [kmol/(m² · s)], W_k is the molecular weight, and P' is the perimeter of the chemically active wall. Neglecting wall interaction terms and accounting for injected air, the species conservation reduces to:

$$\frac{dY_k}{dz} = \frac{\beta_{\text{air,in}}(Y_{k,\text{in}} - Y_k)}{\rho_{\text{gas}} u A_{\text{SZ}}} + \frac{\dot{\omega}_k W_k}{\rho_{\text{gas}} u} \quad (15)$$

where, A_{SZ} is the cross-sectional area of the secondary zone, and $Y_{k,\text{in}}$ refers to the inlet mass fraction of species k . The thermal behavior of the gas is governed by the energy equation, derived from the general PFR energy balance:

$$\rho u A_{\text{SZ}} c_p \frac{dT}{dz} = -A_{\text{SZ}} \sum_{k=1}^K h_k \dot{\omega}_k W_k - P' \sum_{k=1}^K h_k \dot{s}_k W_k + U P(T_w - T) \quad (16)$$

where T is the gas temperature, U is the heat transfer coefficient [W/(m · K)], T_w is the wall temperature, h_k is the specific enthalpy of species k , and P is the perimeter of the wall. By neglecting heat transfer with the wall and including the effects of air injection, the simplified energy equation becomes:

$$\dot{m}_{\text{gas}} c_{p,\text{gas}} \frac{dT}{dz} = -A_{\text{SZ}} \sum_{k=1}^K h_k \dot{\omega}_k W_k + \beta_{\text{air,in}} \left(h_{\text{air,in}} - \sum_{k=1}^K h_k Y_{k,\text{in}} \right) \quad (17)$$

To capture the variable mixing times observed in practical combustor flows, the secondary zone is modeled as two parallel Plug Flow Reactors (PFRs) representing distinct mixing regimes—slow and fast. These dual PFRs simulate the progressive introduction of secondary air into the combustion products, thereby controlling the temperature drop and limiting dissociation effects. Since the incoming air does not immediately achieve full mixing with the hot gases from the primary zone, modeling the system using two separate PFRs offers a realistic depiction of spatial mixing heterogeneity.

After passing through the slow- and fast-mixing paths, the flows are recombined into a joint PFR to achieve uniformity before further cooling by dilution air. The dilution air is injected downstream, within a specific axial segment of the combustor, defined by the normalized coordinates $\ell_{\text{DA,start}}$ and $\ell_{\text{DA,end}}$. The total air addition along the combustor length is described by the local axial air injection rate $\beta_{\text{air,in}}$ [kg/(m · s)], given by:

$$\beta_{\text{air,in}} = \begin{cases} \beta_{\text{SA,SM}}, & \text{if } 0 \leq z \leq l_{\text{SA,SM}} L_{\text{SZ}} \\ \beta_{\text{SA,FM}}, & \text{if } 0 \leq z \leq l_{\text{SA,FM}} L_{\text{SZ}} \\ \beta_{\text{DA}}, & \text{if } l_{\text{DA,start}} L_{\text{SZ}} \leq z \leq l_{\text{DA,end}} L_{\text{SZ}} \\ 0, & \text{otherwise} \end{cases} \quad (18)$$

The magnitudes of air injection rates for each region are defined as:

$$\beta_{SA,SM} = \frac{f_{air,SA} f_{SM} \dot{m}_{air}}{l_{SA,SM} L_{SZ}}, \quad \beta_{SA,FM} = \frac{f_{air,SA} f_{FM} \dot{m}_{air}}{l_{SA,FM} L_{SZ}}, \quad \beta_{DA} = \frac{f_{air,DA} \dot{m}_{air}}{(l_{DA,end} - l_{DA,start}) L_{SZ}} \quad (19)$$

where, f_{SM} and $f_{FM} = 1 - f_{SM}$ represent the fractions of secondary air introduced through the slow and fast mixing paths, respectively. The total portion of air designated for secondary combustion ($f_{air,SA}$) is calculated from the secondary zone design equivalence ratio $\phi_{SZ,des}$ as follows:

$$f_{air,SA} = \frac{\dot{m}_{fuel,takeoff}}{\phi_{SZ,des} \cdot FAR_{st} \cdot \dot{m}_{air,takeoff}} \quad (20)$$

After accounting for primary and secondary zone air fractions, the remaining air is allocated for dilution and its fraction is computed as:

$$f_{air,DA} = 1 - f_{air,PZ} - f_{air,SA} \quad (21)$$

The combustor CRN (Chemical Reactor Network) model is designed to simulate combustion processes and evaluate emissions by accepting a set of defined inputs and generating corresponding outputs. Key input parameters include combustor inlet conditions, such as temperature, pressure, and air mass flow rate, as well as the fuel-to-air ratio. The model also accounts for combustor geometry and incorporates a kinetic mechanism that governs the chemical reactions specific to the fuel type. A detailed summary of these inputs is provided in Table 9. Based on these inputs, the model computes a range of thermo-chemical outputs at the combustor exit, including the stagnation temperature, pressure, enthalpy, and the post-combustion fuel-to-air ratio. Furthermore, it estimates the Emission Indices (EIs) for key species such as CO₂, H₂O, NO_x, and CO. Figure 10 presents a cross-sectional schematic of an RQL burner, with directional arrows used to contextualize the upcoming plots. The green arrow indicates the direction of increasing equivalence ratio (ϕ) in the Primary Zone, which corresponds to the horizontal axis in plots of PZ parameters versus ϕ . The red arrow indicates the direction of increasing axial position along the combustor length, used in plots of Secondary Zone parameters versus percentage length of the SZ.

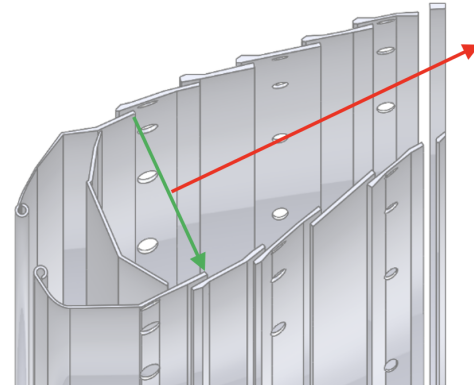


Fig. 10 RQL burner section schematic:
Green arrow indicates primary zone results,
Red arrow indicates secondary zone results.

Engine emissions certification is typically based on the ICAO Landing and Take-Off (LTO) cycle [14], which includes four standardized operating modes representing aircraft behavior near airports. Each mode is defined by a specific thrust setting and time duration, as outlined in Table 8. Emissions are then measured and the results are published in publicly accessible engine emissions databank.

Table 8 ICAO engine emission certification LTO cycle parameters [14].

LTO Phase	Time-in-Mode [min]	Thrust Setting [%]
Take-off	0.7	100
Climb	2.2	85
Approach	4.0	30
Idle	26.0	7

A comparison between the proposed modeling approach and accepted Take-off ICAO LTO values for the CFM56-7B engine [48] [5] [49] for conventional jet fuel is provided in Table 10.

Table 9 CFM56-7B RQL burner simulation inputs at T/O: (a) Burner physical parameters, (b) Burner computational parameters, (c) Fuel and air properties, (d) Mission properties.

(a) Burner physical parameters		(c) Fuel and air properties	
Parameter	Value	Parameter	Value
Combustor Volume [m ³]	0.0023	Stoich. Fuel-to-Air Ratio [-]	0.068
Combustor Length [m]	0.2	Heat of Vaporization [J/kg]	360000
Primary Zone Length [m]	0.05	Fuel Temperature [K]	298.15
Primary Zone Mixing Parameter [-]	0.39	Fuel Pressure [Pa]	101325
Design Equivalence Ratio (PZ) [-]	1.71	Fuel composition [mol frac.]	NC12H26: 0.404 IC8H18: 0.295 TMBENZ: 0.073 NPBENZ: 0.228 C10H8: 0.02
Design Equivalence Ratio (SZ) [-]	0.54	Air composition [mol frac.]	O ₂ : 0.2095 N ₂ : 0.7809 Ar: 0.0096
Slow Mode Fraction [-]	0.2		
Secondary Air Length Fraction (SM) [-]	0.4		
Secondary Air Length Fraction (FM) [-]	0.1		
Dilution Air Start Fraction [-]	0.95		
Dilution Air End Fraction [-]	1.0		
Joint Mixing Fraction [-]	0.8		

(b) Burner computational parameters		(d) Mission properties	
Parameter	Value	Parameter	Value
Fuel [-]	Jet-A1	Burner Inlet Air Temperature [K]	872
Oxidizer [-]	Air	Burner Inlet Air Pressure [Pa]	3338000
Number of PSRs in Primary Zone [-]	41	Air Mass Flow Rate [kg/s]	56.8
Number of Discretizations in SZ [-]	500	Fuel-to-Air Ratio [-]	0.0226

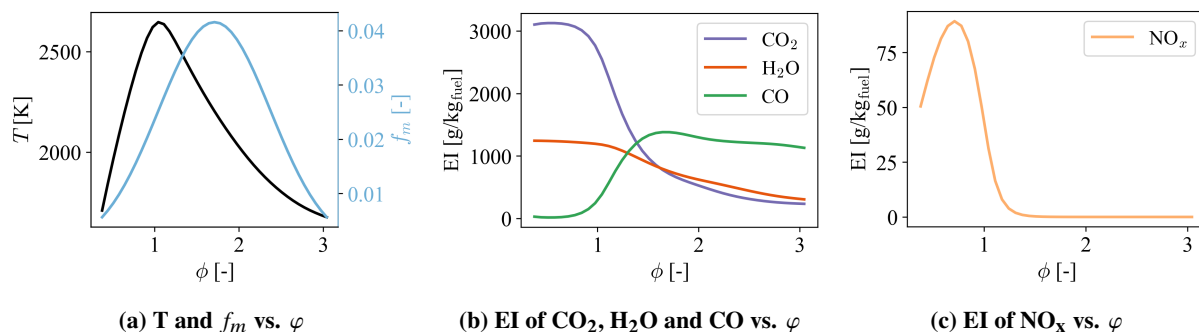


Fig. 11 Primary zone results including temperature, mass fraction, and emission indices for major species.

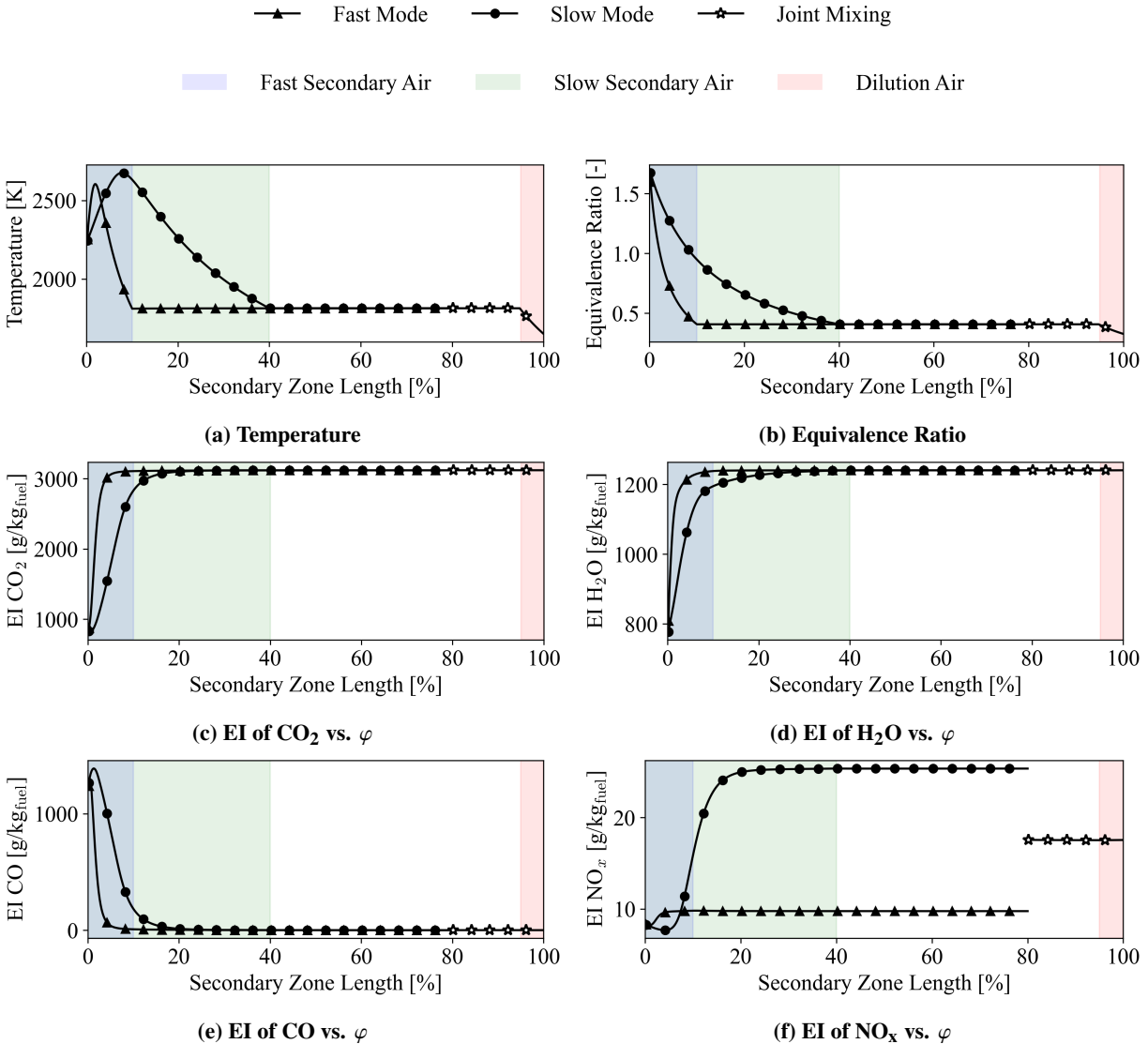


Fig. 12 Secondary Zone results.

Table 10 CFM56-7B burner simulation results at Take-off conditions: Comparison between ICAO LTO data [50] and RCAIDE model predictions. Values in parentheses represent percentage error relative to ICAO LTO data.

Source	EI _{CO₂} [kg _{emissions} /kg _{fuel}]	EI _{H₂O} [kg _{emissions} /kg _{fuel}]	EI _{NO_x} [kg _{emissions} /kg _{fuel}]	EI _{CO} [kg _{emissions} /kg _{fuel}]
ICAO LTO (T/O)	3.16	1.23	0.0174	0.000160
RCAIDE (T/O)	3.11 (-1.68%)	1.24 (+0.52%)	0.0174 (-0.02%)	0.000231 (+44.38%)

F. Fuel Modeling

The key properties utilized to define each fuel within the combustion modeling framework are summarized in Table 11. These parameters include the stoichiometric fuel-to-air ratio, heat of vaporization, temperature and pressure at injection. The table also reports the fuel-to-air ratio (FAR) at takeoff, which was determined through a sensitivity analysis described in Section IV.

Table 11 Fuel and air properties for LH₂, LPG, and LNG used in combustion modeling.

Parameter	LH ₂	LPG	LNG
Stoich. Fuel-to-Air Ratio [-]	0.0285	0.0645	0.0581
Takeoff Fuel-to-Air Ratio [-]	0.00929	0.02162	0.02015
Heat of Vaporization [J/kg]	445000	356000	510000
Fuel Temperature [K]	20	298	111
Fuel Pressure [Pa]	101325	810600	101325

IV. Alternative Fuels Utilization Scenarios

The methodology developed in Section III enables the evaluation of how different energy carriers influence key performance metrics, including direct emissions and operational characteristics. Specifically, this section investigates two levels: Section IV.A discusses fuel substitution effects at the combustor level, which captures changes in emissions resulting from the replacement of conventional fuels with alternatives. Section IV.B demonstrates the operational impact at the fleet level, which accounts for variations in fuel consumption and emissions across the U.S. domestic aviation network.

A. Fuel substitution

1. Emissions Impact

By leveraging the RQL combustor model, burner performance is evaluated under standardized LTO takeoff conditions for each alternative fuel, bench-marked against conventional jet fuel. As shown in Figure 13, simulation results in the primary zone reveal that Liquid Hydrogen (LH₂) produces elevated emissions of H₂O and NO_x at lower equivalence ratios. Across all other fuels, leaner mixtures also correlate with increased CO₂ emissions, while richer mixtures result in higher CO emissions for Liquefied Natural Gas (LNG) and Liquefied Petroleum Gas (LPG). Peak flame temperatures occur near stoichiometric conditions, with LH₂ yielding the highest temperature among the fuels evaluated. The evolution of burner parameters along the length of the secondary zone is illustrated in Figure 14. Across both the fast and slow secondary air mixing regions, the alternative energy carriers exhibit distinct parameter values, yet follow qualitatively similar trends. The final emission indices at the burner exit for each fuel are summarized in Table 12.

Table 12 Emission indices for various fuels at takeoff conditions. Percentage differences in parentheses are relative to Jet-A1.

Fuel	EI _{CO₂} [kg _{emissions} /kg _{fuel}]	EI _{H₂O} [kg _{emissions} /kg _{fuel}]	EI _{NO_x} [kg _{emissions} /kg _{fuel}]	EI _{CO} [kg _{emissions} /kg _{fuel}]
Jet-A1	3.11	1.24	0.0174	0.000231
LH ₂	0.000	8.21 (+562.10%)	0.0539 (+208.00%)	0.000
LPG	2.96 (-5.00%)	1.60 (+28.71%)	0.0154 (-12.00%)	0.000210 (-12.50%)
LNG	2.74 (-12.00%)	2.20 (+77.26%)	0.0126 (-28.00%)	0.000150 (-37.50%)

2. Sensitivity Analysis

To evaluate the influence of different energy carriers on burner performance, a sensitivity analysis was conducted by varying the inlet fuel-to-air ratio. The primary objective of this investigation is to determine the fuel-specific inlet conditions required to maintain consistent combustor performance, particularly with respect to peak temperature, pressure, and turbine inlet temperature (TIT) across a range of alternative fuels. This ensures that the thermal and mechanical loads experienced by the burner itself and the downstream turbine components remain within acceptable design margins, thereby preserving the integrity of the system.

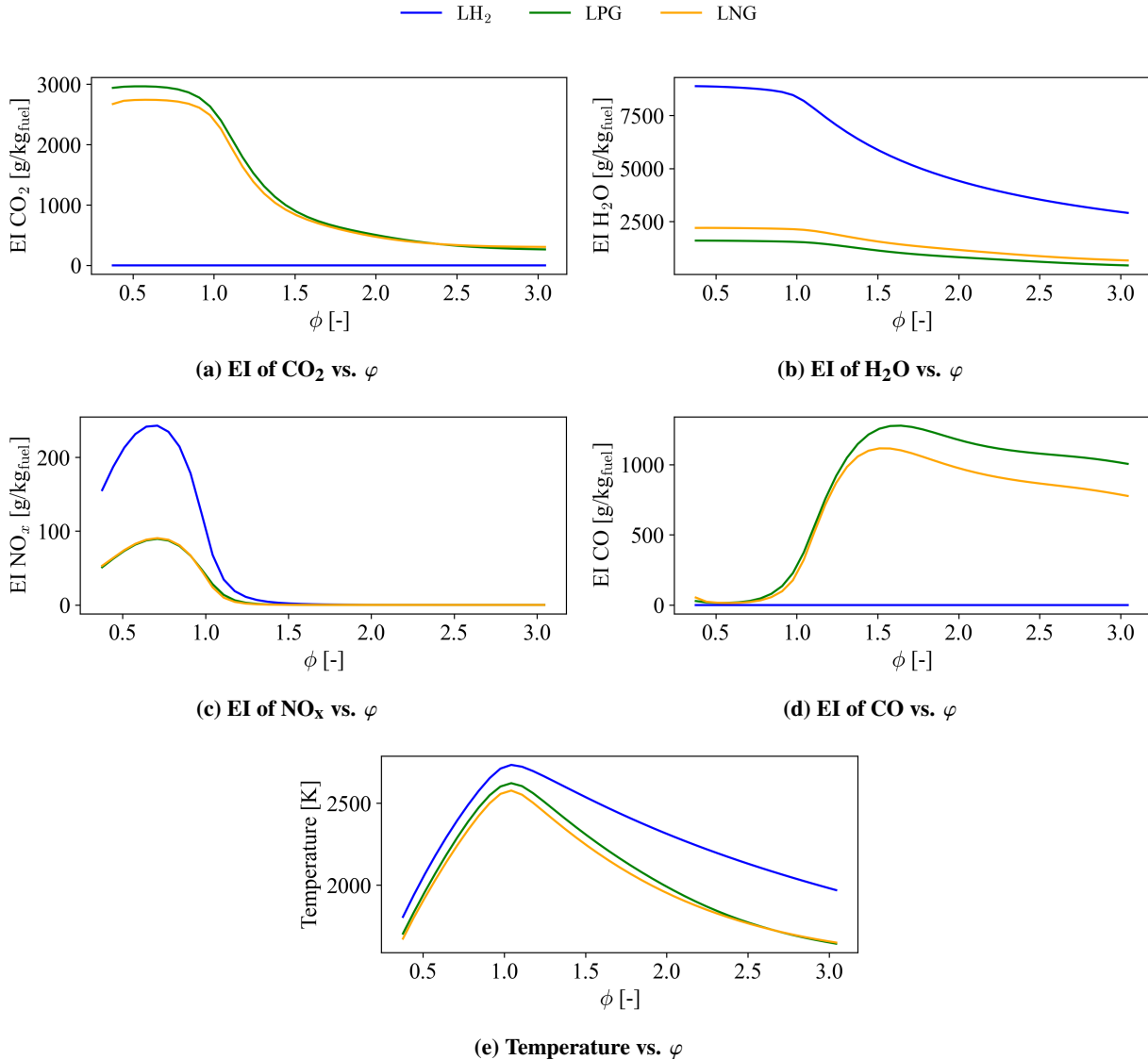


Fig. 13 Primary Zone results for LH₂, LPG and LNG.

From a practical standpoint, this study simulates the scenario in which only the fuel injector is modified to accommodate different fuels, while the gas turbine engine, particularly the burner geometry and the downstream turbine remain unchanged. This allows for the assessment of tank-to-wake emissions and fuel utilization without altering the overall architecture of the propulsion system. Figure 15 illustrates the impact of varying the fuel-to-air ratio on turbine inlet temperature. These results highlight the necessity of fuel-specific tuning to achieve performance matching across different energy carriers. Correspondingly, the variation of FAR has an impact on the final EI of each species, as shown in Figure 16. The values of Fuel-to-Air ratio that were selected to guarantee matching with a jet fuel Turbine Inlet Temperature of 1650.87 K are reported in Table 13.

Table 13 Selected Fuel-to-Air Ratios matching the jet fuel Turbine Inlet Temperature for different energy carriers.

Parameter	LH ₂	LPG	LNG
FAR [-]	0.00929	0.02162	0.02015

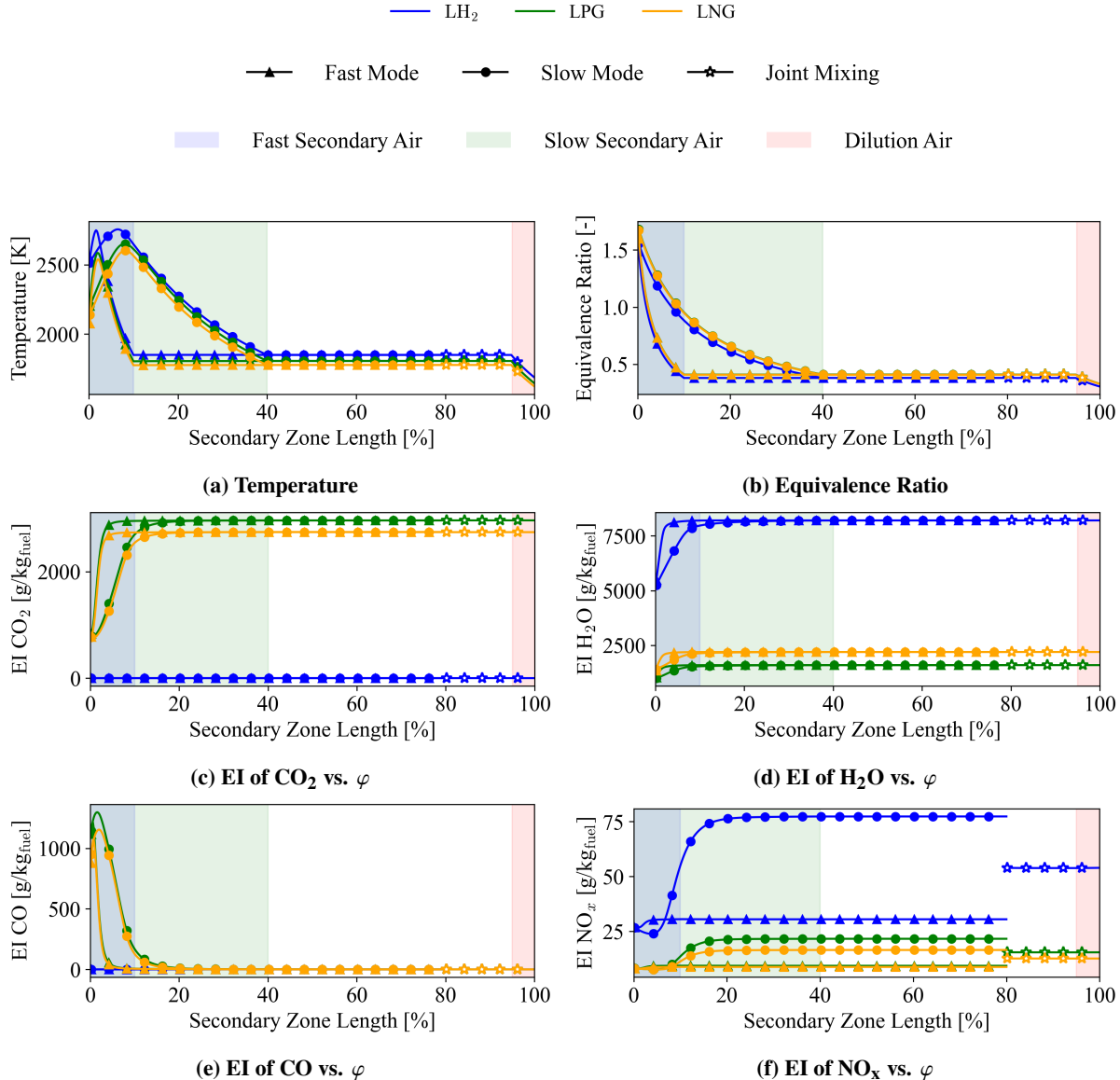


Fig. 14 Secondary Zone results for different fuels.

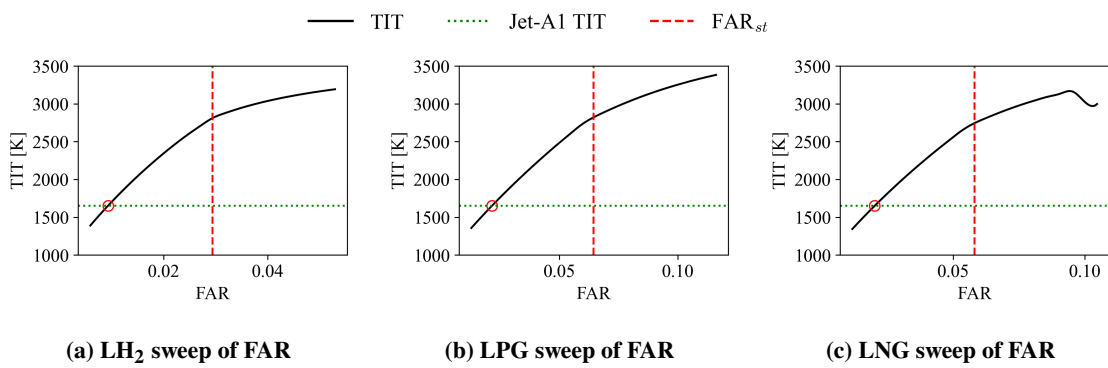


Fig. 15 Effect of Fuel-to-Air ratio variation on Turbine Inlet Temperature.

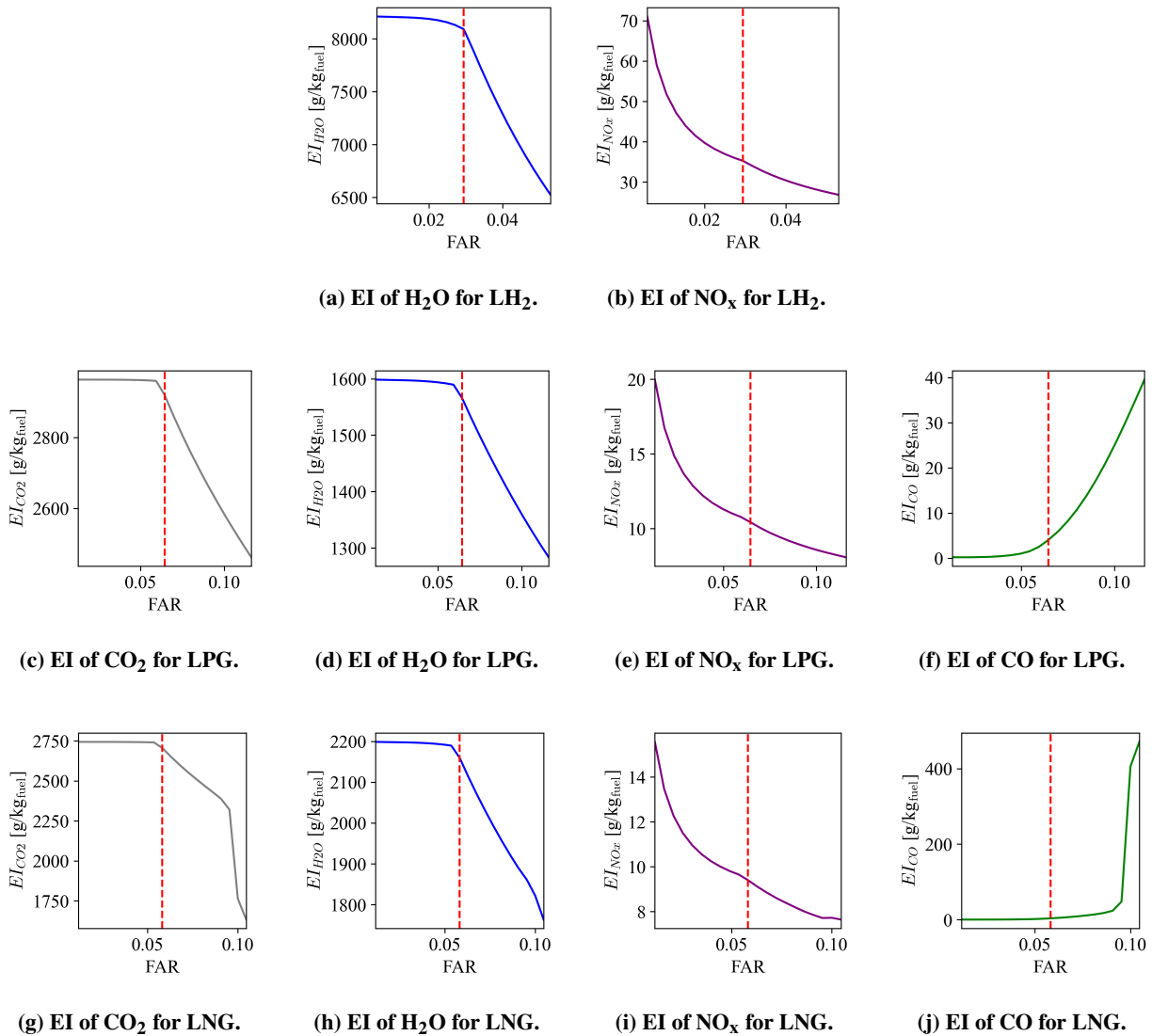


Fig. 16 Emission Index sensitivity analysis for LH_2 , LPG, and LNG. The red dashed line indicates the stoichiometric Fuel-to-Air ratio of each fuel.

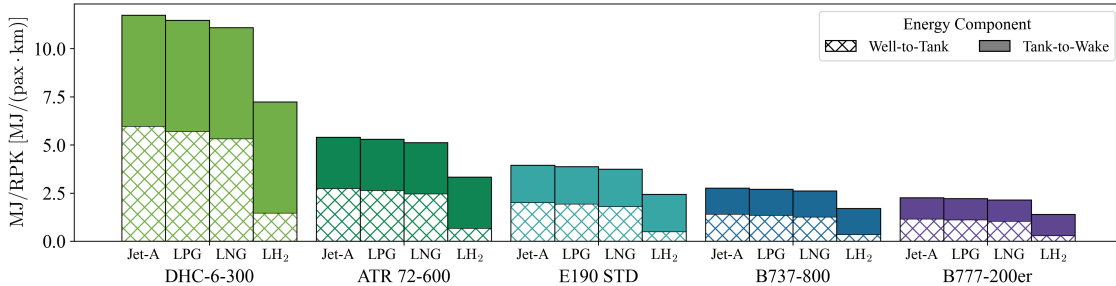
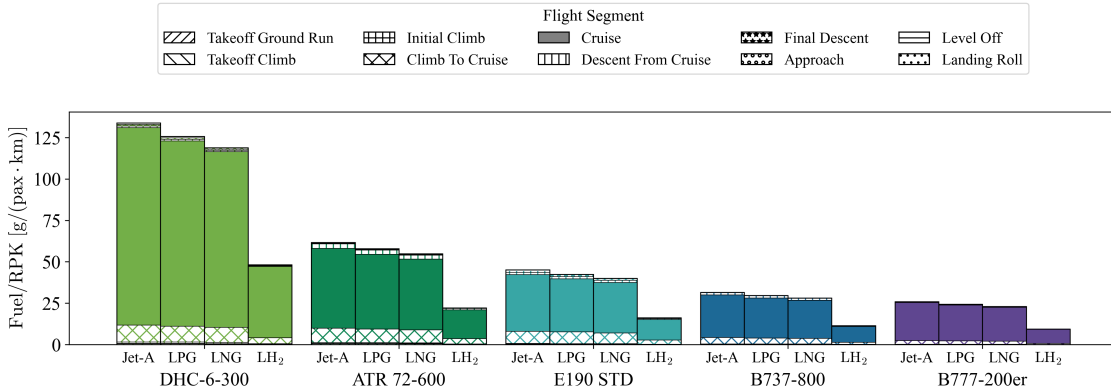
B. Domestic Flight Operations

1. Energy and Fuel Demand

Two key performance metrics are used to evaluate the energy and fuel requirements of each aircraft class: energy consumption per Revenue Passenger Kilometer (MJ/RPK) and fuel consumption per Revenue Passenger Kilometer (Fuel/RPK). Table 14 presents the annual MJ/RPK values for U.S. domestic operations, based on data from the 2019 Bureau of Transportation Statistics [37]. Correspondingly, Figure 17 illustrates the normalized Well-to-Wake energy consumption across different energy carriers and aircraft classes. The figure distinguishes between the Tank-to-Wake and Well-to-Tank contributions. Notably, the assumption of fixed mission energy across fuels for a given aircraft category results in a constant Tank-to-Wake component. In contrast, the Well-to-Tank energy requirement decreases progressively from Jet-A to LPG, LNG, and LH_2 . This trend is consistent across all aircraft classes, with larger aircraft exhibiting lower energy consumption per RPK.

Table 14 Annual U.S. domestic energy consumption per Revenue Passenger Kilometer for each aircraft class.

Metric	DHC-6-300	ATR 72-600	E190 STD	B737-800	B777-200er
MJ/RPK	5.7816	2.6673	1.9477	1.3633	1.1187

**Fig. 17 Annual U.S. Domestic MJ/RPK by aircraft class and fuel.****Fig. 18 Annual U.S. Domestic Fuel/RPK by aircraft class and fuel.**

The corresponding values of annual U.S. domestic Fuel/RPK across the selected classes of aircraft and fuel types, segmented by flight phase, are reported in Figure 18. The results exhibit consistent trends in fuel utilization, with the cruise segment accounting for the largest proportion of total fuel consumption, followed by the climb to cruise segment across all aircraft and fuel combinations. Despite operating the highest number of routes and transporting the largest passenger volumes, the B737-800 demonstrates a lower Fuel/RPK compared to smaller aircraft such as the DHC-6-300 and ATR 72-600. For alternative fuels, fuel mass values have been adjusted using the ratio of kerosene specific energy to that of the respective fuel. Among the alternative fuels considered, Liquefied Petroleum Gas (LPG) and Liquefied Natural Gas (LNG) show a modest reduction in Fuel/RPK relative to Jet-A. Notably, Liquid Hydrogen (LH₂) consistently achieves the lowest Fuel/RPK values across all aircraft classes.

2. Direct Emissions

The annual U.S. direct emissions for the five selected aircraft classes are evaluated using nominal mission simulations conducted within the RCAIDE framework. The emission indices for each species, flight segment, and fuel type, derived from the Boeing 737-800 simulation, are presented in Table 15. Corresponding EI values for the DHC-6-300, ATR 72-600, E190 STD, and B777-200ER are available in Appendix B. From these results, the annual U.S. domestic gCO_{2e}/RPK can be derived for each aircraft class, fuel type, and emission species, as illustrated in Figure 19. Across all charts, an inverse correlation is observed between aircraft capacity and gCO_{2e} per revenue passenger-kilometer, with larger aircraft consistently exhibiting lower emissions per RPK. In terms of flight segments, the cruise phase contributes the most significantly to overall emissions, followed by the climb to cruise and descent from cruise phases.

Table 15 Emission Indices for the Boeing 737-800 mission.

(a) EI _{CO₂}					(d) EI _{H₂O}				
Segment	Jet-A	LH ₂	LNG	LPG	Segment	Jet-A	LH ₂	LNG	LPG
Takeoff Run	3.01686	0.000	2.70509	2.92872	Takeoff Run	1.19484	7.85395	2.06994	1.57660
Takeoff Climb	3.01342	0.000	2.70193	2.92599	Takeoff Climb	1.19345	7.85126	2.06742	1.57478
Initial Climb	3.01245	0.000	2.70104	2.92519	Initial Climb	1.19306	7.85047	2.06672	1.57426
Climb to Cruise	2.66958	0.000	2.26316	2.68358	Climb to Cruise	1.19993	7.88595	2.02149	1.57860
Cruise	3.06201	0.000	2.74382	2.94057	Cruise	1.21757	7.89796	2.11251	1.60269
Descent from Cruise	3.04181	0.000	2.35533	2.71991	Descent from Cruise	1.20840	7.88138	2.08064	1.57970
Final Descent	3.02646	0.000	2.71397	2.93504	Final Descent	1.19891	7.86183	2.07741	1.58172
Approach	3.01625	0.000	2.70455	2.92827	Approach	1.19460	7.85350	2.06953	1.57630
Level Off	3.01431	0.000	2.70275	2.92673	Level Off	1.19381	7.85197	2.06807	1.57525
Landing Roll	3.01712	0.000	2.70533	2.92894	Landing Roll	1.19494	7.85415	2.07013	1.57674

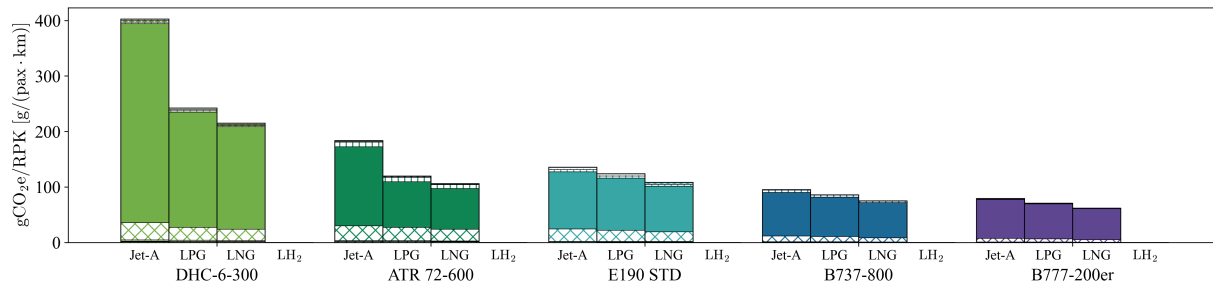
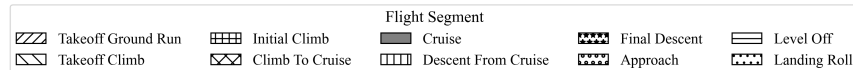
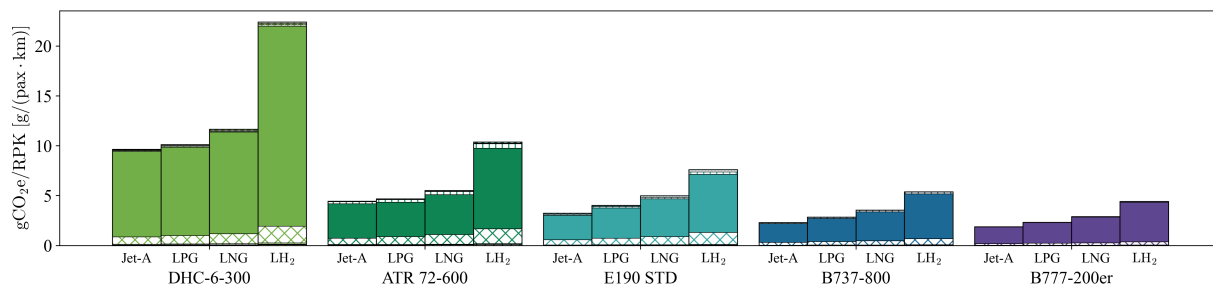
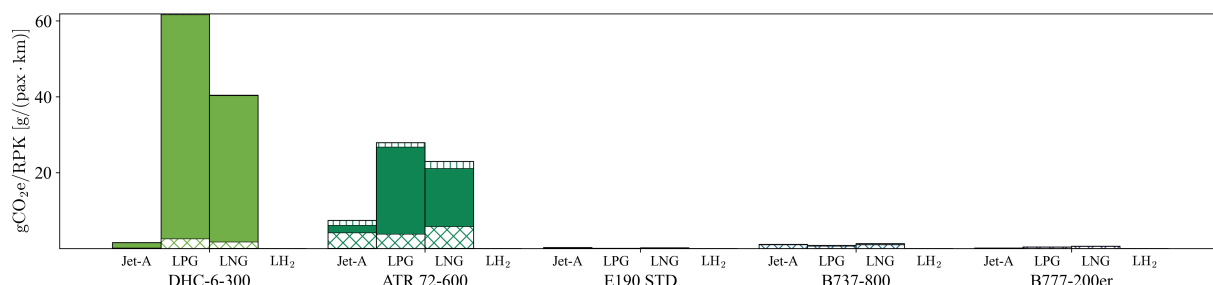
(c) EI _{NO_x}					(b) EI _{CO}				
Segment	Jet-A	LH ₂	LNG	LPG	Segment	Jet-A	LH ₂	LNG	LPG
Takeoff Run	1.447e-2	5.536e-2	1.228e-2	1.082e-2	Takeoff Run	5.940e-4	0.000	2.720e-4	2.420e-4
Takeoff Climb	1.486e-2	5.652e-2	1.261e-2	1.112e-2	Takeoff Climb	5.790e-4	0.000	2.630e-4	2.340e-4
Initial Climb	1.496e-2	5.683e-2	1.270e-2	1.120e-2	Initial Climb	5.830e-4	0.000	2.653e-4	2.320e-4
Climb to Cruise	1.070e-2	4.350e-2	9.181e-3	7.910e-3	Climb to Cruise	2.415e-1	0.000	2.705e-1	1.568e-1
Cruise	8.067e-3	3.584e-2	6.995e-3	5.792e-3	Cruise	6.367e-3	0.000	5.470e-3	2.773e-3
Descent from Cruise	1.070e-2	4.384e-2	9.192e-3	7.865e-3	Descent from Cruise	4.376e-3	0.000	2.388e-1	1.368e-1
Final Descent	1.326e-2	5.184e-2	1.129e-2	9.861e-3	Final Descent	8.937e-4	0.000	4.474e-4	3.200e-4
Approach	1.450e-2	5.550e-2	1.231e-2	1.084e-2	Approach	6.261e-4	0.000	2.890e-4	2.468e-4
Level Off	1.476e-2	5.622e-2	1.252e-2	1.104e-2	Level Off	5.864e-4	0.000	2.673e-4	2.367e-4
Landing Roll	1.444e-2	5.527e-2	1.225e-2	1.080e-2	Landing Roll	5.957e-4	0.000	2.731e-4	2.429e-4

Figure 19a isolates the contribution of CO₂ to total gCO_{2e}/RPK. Among the fuels analyzed, conventional Jet-A consistently results in the highest CO₂ emissions, with its impact being more pronounced in lower-capacity aircraft classes. Liquefied petroleum gas (LPG) and liquefied natural gas (LNG) exhibit progressively lower CO₂ emission levels, with these benefits being especially evident in regional aircraft. As expected, liquid hydrogen (LH₂) yields negligible CO₂ emissions.

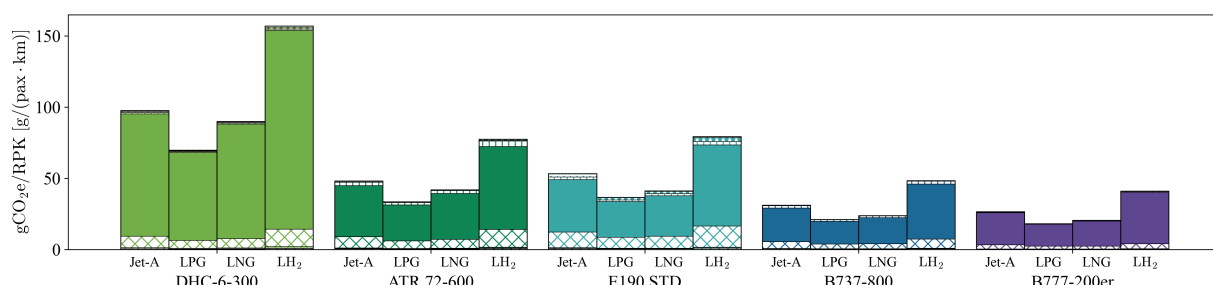
In contrast, emissions associated with water vapor (H₂O) are greatest for LH₂, followed in order by LNG, LPG, and Jet-A, across all aircraft classes. As shown in Figure 19b, this trend remains consistent regardless of aircraft size. While LH₂ offers significant decarbonization potential by eliminating direct CO₂ emissions, its increased water vapor output raises concerns regarding non-CO₂ climate effects, particularly Aviation Induced Cloudiness (AIC), which is known to contribute to radiative forcing. Carbon monoxide (CO) emissions exhibit greater variability across aircraft classes, with elevated levels observed in smaller regional aircraft and significantly lower values in larger platforms. Across all aircraft in Figure 19c, CO emissions are consistently negligible when operating on LH₂.

In terms of nitrogen oxides (NO_x), Figure 19d shows that liquid hydrogen exhibits the highest emissions among all fuel types, followed by Jet-A, LNG, and LPG. This trend is preserved across all aircraft classes, although the absolute magnitude of NO_x emissions decreases with increasing aircraft size. The elevated NO_x emissions associated with LH₂ represent a significant tradeoff in its implementation, while LPG and LNG consistently yield the lowest NO_x emissions, positioning them as favorable transitional fuels to mitigate nitrogen oxides production. It is important to note, however, that the current model assumes a fixed flame temperature for all fuels, which contributes to the higher NO_x values observed for LH₂. In reality, hydrogen combustion allows for lower equivalence ratios due to its higher flame stability and blow-off limits, enabling a reduction in flame temperature and consequently in NO_x formation.

Finally, Figure 20 illustrates the total Well-to-Wake greenhouse gas (GHG) emissions, expressed in gCO_{2e}/RPK, for each aircraft-fuel combination. These values are calculated as the sum of the Well-to-Tank and Tank-to-Wake contributions. The results confirm a consistent reduction in gCO_{2e}/RPK with increasing aircraft capacity. Among the fuels analyzed, Jet-A consistently shows the highest emission intensity across all classes, followed sequentially by LPG, LNG, and LH₂. Notably, the Well-to-Tank contribution for LH₂ is zero due to the assumed renewable production pathway, and becomes increasingly negligible for other fuels as aircraft size increases. The negative bars in the figure represent the feedstock credit, which partially offsets the overall GHG impact by accounting for carbon capture or renewable sourcing in the upstream production phase.

(a) CO₂ emissions by aircraft class and fuel.(b) H₂O emissions by aircraft class and fuel.

(c) CO emissions by aircraft class and fuel.

(d) NO_x emissions by aircraft class and fuel.**Fig. 19** Annual U.S. Domestic gCO₂e/RPK by emission species, aircraft class and fuel type.

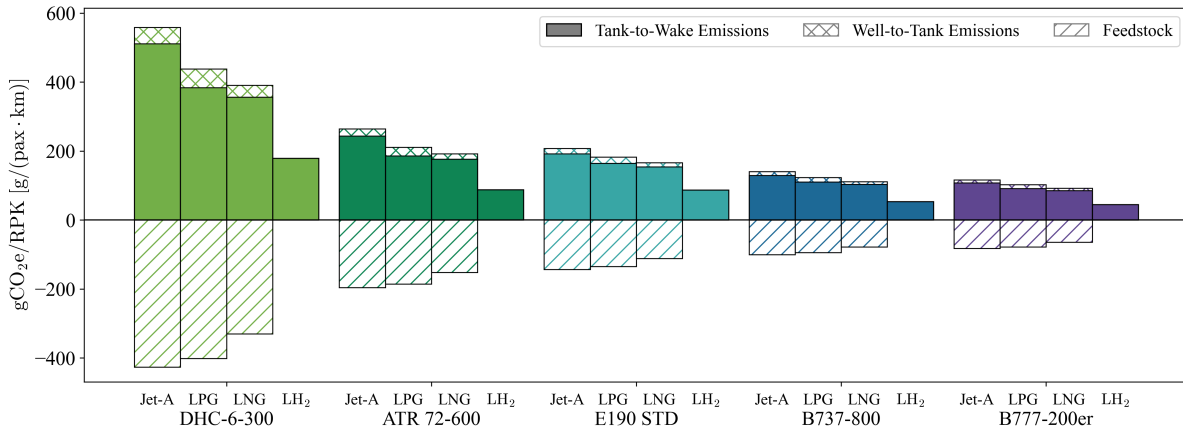


Fig. 20 Total annual U.S. domestic gCO₂e/RPK by aircraft class and fuel.

V. Conclusion

This study presented an energy and emissions-based evaluation of deploying three alternative fuels in the current U.S. domestic network: liquid hydrogen (LH₂), liquefied petroleum gas (LPG), and liquefied natural gas (LNG). Simulations were conducted for five representative classes of transport aircraft, using RCAIDE, a multifidelity framework for preliminary aircraft design and analysis [26]. The analysis quantified direct emissions associated with each fuel production and operation, assuming fixed aircraft configuration and performance across all scenarios to isolate the effects of fuel-specific properties.

At the combustor level, a high-fidelity Chemical Reactor Network (CRN) model of a Rich-Burn, Quick-Mix, Lean-Burn (RQL) combustor was employed to estimate fuel-specific emission indices under representative engine operating conditions. Results showed that LH₂ yields negligible emissions of CO₂ and CO, but results in significantly higher emissions of H₂O and NO_x. LPG demonstrated modest reductions in CO₂, NO_x, and CO emissions relative to Jet-A, but slightly higher H₂O output. Similarly, LNG exhibited minor emissions of CO₂, NO_x, and CO compared to LPG, with a slightly higher production of H₂O.

At the mission level, larger aircraft classes were found to have lower energy consumption and fuel burn per Revenue Passenger Kilometer (RPK), with LH₂ requiring the least fuel mass per RPK, followed by LNG, LPG, and Jet-A. In terms of annual U.S. domestic emissions, Jet-A consistently resulted in the highest CO₂ emissions, particularly for regional aircraft. LPG and LNG showed progressively lower CO₂ outputs, while LH₂ demonstrated near-zero CO₂ emissions. Conversely, H₂O emissions were highest for LH₂, followed by LNG, LPG, and Jet-A. CO emissions exhibited greater variability across aircraft classes, with higher levels in smaller aircraft and limited levels under LH₂ combustion. For nitrogen oxides (NO_x), LH₂ was associated with the highest emissions, followed by Jet-A, LNG, and LPG. These trends are further reflected in the aggregated gCO₂e/RPK values, which account for the global warming potential of each species. A consistent decrease in total climate impact is observed with increasing aircraft size. Among the fuels, Jet-A exhibits the highest total gCO₂e/RPK across all aircraft classes, followed by LPG, LNG, and LH₂. For Jet-A, LPG, and LNG, CO₂ is the primary contributor to total climate impact, while for LH₂, NO_x emissions dominate the overall gCO₂e/RPK.

Future work should account for the emissions associated with fuel transportation and liquefaction. Additionally, the integration of these fuels into current aircraft platforms warrants further investigation, including modifications to powerplant design and overall aircraft weight and performance. An assessment of these integration effects will be essential to evaluate the environmental impact and operational feasibility of transitioning to alternative fuels.

Overall, this work offers a quantitative assessment the tradeoffs and potential advantages of deploying alternative fuels within the current U.S. domestic aviation fleet. By isolating the influence of fuel-specific properties, the study aims to inform strategic decisions aimed at supporting the transition toward more sustainable air transportation systems.

Acknowledgments

This research work was funded by The Boeing Company under the Grant: Renewable Energy Pathways and Novel Propulsion Systems for Sustainable Aircraft Concepts (2024-ETT-PA-102). The authors would like to thank our research collaborators from The Boeing Company Dr. Dominic Barone and Hubert Wong, for their guidance during the development of this study.

Appendix

A. Mission Profiles

Table 16 Flight profile segments for the remaining four aircraft modeled in this study.

(a) DHC-6-300

Segment	Altitude [ft]	Airspeed [kt]	Rate
Takeoff Ground Run	0	0–70	Friction Coef: 0.03
Takeoff Climb	0–35	70–80	150 fpm
Initial Climb	35–1,000	130	1,000 fpm
Climb to Cruise	1,000–10,000	130–140	600 fpm
Cruise	10,000	150	Distance: 1200 km
Descent from Cruise	10,000–3,000	140	–1,000 fpm
Final Descent	3,000–1,500	120	–400 fpm
Approach	1,500–50	100	–300 fpm
Level Off	50–0	80	–200 fpm
Landing Roll	0	80–10	Friction Coef: 0.4

(b) ATR 72-600

Segment	Altitude [ft]	Airspeed [kt]	Rate
Takeoff Ground Run	0	0–110	Friction Coef: 0.03
Takeoff Climb	0–35	110–140	130 fpm
Initial Climb	35–1,000	180	1,000 fpm
Climb to Cruise	1,000–20,000	180	1,000 fpm
Cruise	20,000	375	Distance: 1300 km
Descent from Cruise	20,000–3,000	180	–600 fpm
Final Descent	3,000–1,500	180	–600 fpm
Approach	1,500–50	150	–300 fpm
Level Off	50–0	110	–200 fpm
Landing Roll	0	110–10	Friction Coef: 0.4

(c) E190 STD

Segment	Altitude [ft]	Airspeed [kt]	Rate
Takeoff Ground Run	0	0–150	Friction Coef: 0.03
Takeoff Climb	0–35	150–180	200 fpm
Initial Climb	35–1,000	200	1,200 fpm
Climb to Cruise	1,000–35,000	200–400	1,000 fpm
Cruise	35,000	430	Distance: 3000 km
Descent from Cruise	35,000–10,000	300	–1,200 fpm
Final Descent	10,000–2,000	200	–400 fpm
Approach	2,000–50	160	–500 fpm
Level Off	50–0	150	–300 fpm
Landing Roll	0	150–10	Friction Coef: 0.4

(d) B777-200er

Segment	Altitude [ft]	Airspeed [kt]	Rate
Takeoff Ground Run	0	0–180	Friction Coef: 0.03
Takeoff Climb	0–35	180–120	200 fpm
Initial Climb	35–1,000	230	1,500 fpm
Climb to Cruise	1,000–40,000	230–350	1,300 fpm
Cruise	40,000	490	Distance: 7500 km
Descent from Cruise	40,000–10,000	330	–1,500 fpm
Final Descent	10,000–2,000	250	–500 fpm
Approach	2,000–50	190	–500 fpm
Level Off	50–0	180	–300 fpm
Landing Roll	0	160–10	Friction Coef: 0.4

B. Emission Indices

Table 17 Emission Indices for the DHC-6-300 aircraft.

(a) EI_{CO₂}

Segment	Jet-A	LH ₂	LNG	LPG
Takeoff Run	3.00176	0.000	2.69399	2.91523
Takeoff Climb	3.00132	0.000	2.69355	2.91506
Initial Climb	3.00603	0.000	2.69317	2.91489
Climb to Cruise	3.00990	0.000	2.21768	2.38295
Cruise	3.00712	0.000	1.74305	1.85551
Descent from Cruise	3.00387	0.000	2.21764	2.38304
Final Descent	3.00254	0.000	2.69358	2.91523
Approach	3.00198	0.000	2.69382	2.91516
Level Off	3.00232	0.000	2.69370	2.91512
Landing Roll	3.00232	0.000	2.69392	2.91521

(b) EI_{H₂O}

Segment	Jet-A	LH ₂	LNG	LPG
Takeoff Run	1.19471	7.74010	2.07192	1.58097
Takeoff Climb	1.19442	7.73959	2.07140	1.58064
Initial Climb	1.19428	7.73930	2.07117	1.58049
Climb to Cruise	1.19784	7.74633	1.83474	1.44735
Cruise	1.20087	7.75226	1.60129	1.32350
Descent from Cruise	1.19851	7.74759	1.83593	1.44807
Final Descent	1.19575	7.74216	2.07380	1.58208
Approach	1.19490	7.74052	2.07226	1.58116
Level Off	1.19452	7.73977	2.07158	1.58076
Landing Roll	1.19467	7.74002	2.07185	1.58092

(c) EI_{NO_x}

Segment	Jet-A	LH ₂	LNG	LPG
Takeoff Run	7.296e-3	3.154e-2	6.243e-3	5.243e-3
Takeoff Climb	7.338e-3	3.169e-2	6.280e-3	5.274e-3
Initial Climb	7.349e-3	3.173e-2	6.291e-3	5.282e-3
Climb to Cruise	6.800e-3	2.992e-2	6.437e-3	5.039e-3
Cruise	6.331e-3	2.838e-2	6.656e-3	4.838e-3
Descent from Cruise	6.693e-3	2.958e-2	6.346e-3	4.953e-3
Final Descent	7.121e-3	3.099e-2	6.095e-3	5.102e-3
Approach	7.261e-3	3.144e-2	6.214e-3	5.214e-3
Level Off	7.323e-3	3.163e-2	6.267e-3	5.263e-3
Landing Roll	7.302e-3	3.156e-2	6.249e-3	5.248e-3

(d) EI_{CO}

Segment	Jet-A	LH ₂	LNG	LPG
Takeoff Run	7.440e-3	0.000	5.539e-3	1.629e-3
Takeoff Climb	7.433e-3	0.000	5.472e-3	1.627e-3
Initial Climb	7.527e-3	0.000	5.563e-3	1.658e-3
Climb to Cruise	9.703e-3	0.000	1.843e-1	2.624e-1
Cruise	1.163e-2	0.000	3.637e-1	5.281e-1
Descent from Cruise	1.001e-2	0.000	1.851e-1	2.625e-1
Final Descent	8.100e-3	0.000	7.062e-3	1.890e-3
Approach	7.659e-3	0.000	5.880e-3	1.710e-3
Level Off	7.439e-3	0.000	5.496e-3	1.629e-3
Landing Roll	7.438e-3	0.000	5.529e-3	1.629e-3

Table 18 Emission Indices for the ATR72-600 aircraft.

(a) EI_{CO₂}

Segment	Jet-A	LH ₂	LNG	LPG
Takeoff Run	2.99892	0.000	2.67878	2.91685
Takeoff Climb	2.99741	0.000	2.68797	2.91641
Initial Climb	2.99584	0.000	2.68744	2.91583
Climb to Cruise	2.99584	0.000	2.68729	2.91583
Cruise	2.96780	0.000	1.72137	1.82318
Descent from Cruise	2.99811	0.000	2.67738	2.91605
Final Descent	2.99811	0.000	2.68667	2.91605
Approach	2.99777	0.000	2.68791	2.91632
Level Off	2.99747	0.000	2.68788	2.91642
Landing Roll	2.99891	0.000	2.68788	2.91684

(b) EI_{H₂O}

Segment	Jet-A	LH ₂	LNG	LPG
Takeoff Run	1.19527	7.75889	2.07286	1.58127
Takeoff Climb	1.19457	7.75771	2.07167	1.58049
Initial Climb	1.19399	7.75623	2.07065	1.57983
Climb to Cruise	1.19399	7.78480	2.07065	1.57983
Cruise	1.20045	7.76859	1.55833	1.27334
Descent from Cruise	1.19557	7.78480	2.07328	1.58157
Final Descent	1.19557	7.75925	2.07328	1.58157
Approach	1.19506	7.75846	2.07251	1.58103
Level Off	1.19461	7.75779	2.07174	1.58054
Landing Roll	1.19526	7.75888	2.07285	1.58126

(c) EI_{NO_x}

Segment	Jet-A	LH ₂	LNG	LPG
Takeoff Run	7.847e-3	3.396e-2	6.782e-3	5.621e-3
Takeoff Climb	7.916e-3	3.420e-2	6.842e-3	5.675e-3
Initial Climb	8.045e-3	3.464e-2	6.955e-3	5.774e-3
Climb to Cruise	7.912e-3	3.419e-2	7.077e-3	5.670e-3
Cruise	6.527e-3	2.961e-2	6.601e-3	4.913e-3
Descent from Cruise	7.644e-3	3.330e-2	7.077e-3	5.457e-3
Final Descent	7.843e-3	3.397e-2	6.782e-3	5.617e-3
Approach	7.943e-3	3.429e-2	6.866e-3	5.696e-3
Level Off	7.847e-3	3.396e-2	6.782e-3	5.621e-3
Landing Roll	7.847e-3	3.396e-2	6.782e-3	5.621e-3

(d) EI_{CO}

Segment	Jet-A	LH ₂	LNG	LPG
Takeoff Run	1.147e-2	0.000	1.159e-2	2.938e-3
Takeoff Climb	1.142e-2	0.000	1.031e-2	2.893e-3
Initial Climb	1.154e-2	0.000	9.958e-3	2.915e-3
Climb to Cruise	4.679e-1	0.000	7.411e-1	4.529e-1
Cruise	4.069e-2	0.000	3.584e-1	5.098e-1
Descent from Cruise	4.679e-1	0.000	7.411e-1	4.529e-1
Final Descent	1.257e-2	0.000	1.832e-2	3.490e-3
Approach	1.197e-2	0.000	1.259e-2	3.142e-3
Level Off	1.144e-2	0.000	1.041e-2	2.904e-3
Landing Roll	1.147e-2	0.000	1.158e-2	2.938e-3

Table 19 Emission Indices for the Embraer E190 STD aircraft.

(a) EI _{CO₂}					(b) EI _{H₂O}				
Segment	Jet-A	LH ₂	LNG	LPG	Segment	Jet-A	LH ₂	LNG	LPG
Takeoff Run	2.96138	0.000	2.65498	2.88065	Takeoff Run	1.17362	7.77294	2.03207	1.54966
Takeoff Climb	2.95777	0.000	2.65158	2.87686	Takeoff Climb	1.17217	7.77061	2.02942	1.54754
Initial Climb	2.95636	0.000	2.65025	2.87538	Initial Climb	1.17161	7.76964	2.02840	1.54672
Climb to Cruise	2.98944	0.000	2.68158	2.90354	Climb to Cruise	1.18627	7.79429	2.05562	1.56677
Cruise	3.01607	0.000	2.70718	2.92827	Cruise	1.19805	7.81315	2.07758	1.58333
Descent from Cruise	3.00324	0.000	2.69366	2.91260	Descent from Cruise	1.19252	7.80612	2.06707	1.57471
Final Descent	2.97268	0.000	2.66579	2.89239	Final Descent	1.17836	7.78092	2.04081	1.55654
Approach	2.96126	0.000	2.65490	2.88061	Approach	1.17360	7.77294	2.03205	1.54964
Level Off	2.95895	0.000	2.65269	2.87811	Level Off	1.17265	7.77140	2.03030	1.54824
Landing Roll	2.96137	0.000	2.65497	2.88064	Landing Roll	1.17361	7.77293	2.03206	1.54966

(c) EI _{NO_x}					(d) EI _{CO}				
Segment	Jet-A	LH ₂	LNG	LPG	Segment	Jet-A	LH ₂	LNG	LPG
Takeoff Run	1.647e-2	6.184e-2	1.422e-2	1.237e-2	Takeoff Run	1.218e-3	0.000	5.927e-4	1.850e-4
Takeoff Climb	1.692e-2	6.329e-2	1.463e-2	1.274e-2	Takeoff Climb	1.190e-3	0.000	5.738e-4	1.802e-4
Initial Climb	1.709e-2	6.384e-2	1.478e-2	1.287e-2	Initial Climb	1.191e-3	0.000	5.738e-4	1.806e-4
Climb to Cruise	1.296e-2	5.095e-2	1.122e-2	9.627e-3	Climb to Cruise	3.961e-3	0.000	2.503e-3	1.098e-3
Cruise	9.450e-3	4.006e-2	8.200e-3	6.847e-3	Cruise	6.353e-3	0.000	4.136e-3	1.850e-3
Descent from Cruise	1.136e-2	4.588e-2	9.823e-3	8.341e-3	Descent from Cruise	4.898e-3	0.000	3.421e-3	1.473e-3
Final Descent	1.495e-2	5.722e-2	1.291e-2	1.113e-2	Final Descent	1.728e-3	0.000	9.246e-4	2.945e-4
Approach	1.645e-2	6.181e-2	1.421e-2	1.234e-2	Approach	1.280e-3	0.000	6.297e-4	1.969e-4
Level Off	1.677e-2	6.281e-2	1.449e-2	1.261e-2	Level Off	1.206e-3	0.000	5.838e-4	1.830e-4
Landing Roll	1.648e-2	6.184e-2	1.422e-2	1.237e-2	Landing Roll	1.218e-3	0.000	5.927e-4	1.850e-4

Table 20 Emission Indices for the Boeing 777-200er aircraft.

(a) EI _{CO₂}					(b) EI _{H₂O}				
Segment	Jet-A	LH ₂	LNG	LPG	Segment	Jet-A	LH ₂	LNG	LPG
Takeoff Run	3.00891	0.000	2.69775	2.92243	Takeoff Run	1.19178	7.83866	2.06436	1.57301
Takeoff Climb	3.00415	0.000	2.69335	2.91838	Takeoff Climb	1.18986	7.83484	2.06088	1.57045
Initial Climb	3.00165	0.000	2.69104	2.91616	Initial Climb	1.18887	7.83280	2.05907	1.56909
Climb to Cruise	3.03538	0.000	2.25016	2.71240	Climb to Cruise	1.20619	7.86957	1.98889	1.57873
Cruise	3.05464	0.000	2.73948	2.94338	Cruise	1.21335	7.87994	2.10451	1.59891
Descent from Cruise	3.04215	0.000	2.24315	2.70958	Descent from Cruise	1.20969	7.87688	1.96259	1.58292
Final Descent	3.01678	0.000	2.70507	2.92815	Final Descent	1.19510	7.84512	2.07043	1.57725
Approach	3.00748	0.000	2.69645	2.92127	Approach	1.19122	7.83752	2.06335	1.57227
Level Off	3.00512	0.000	2.69425	2.91924	Level Off	1.19025	7.83562	2.06159	1.57097
Landing Roll	3.00974	0.000	2.69852	2.92315	Landing Roll	1.19212	7.83934	2.06496	1.57315

(c) EI _{NO_x}					(d) EI _{CO}				
Segment	Jet-A	LH ₂	LNG	LPG	Segment	Jet-A	LH ₂	LNG	LPG
Takeoff Run	1.470e-2	5.589e-2	1.247e-2	1.102e-2	Takeoff Run	4.820e-4	0.000	2.101e-4	1.719e-4
Takeoff Climb	1.524e-2	5.749e-2	1.292e-2	1.143e-2	Takeoff Climb	4.642e-4	0.000	2.000e-4	1.631e-4
Initial Climb	1.553e-2	5.833e-2	1.316e-2	1.165e-2	Initial Climb	4.598e-4	0.000	1.973e-4	1.592e-4
Climb to Cruise	1.117e-2	4.488e-2	9.623e-3	8.272e-3	Climb to Cruise	3.926e-3	0.000	2.559e-1	1.375e-1
Cruise	8.660e-3	3.771e-2	7.500e-3	6.285e-3	Cruise	4.831e-3	0.000	3.221e-3	1.668e-3
Descent from Cruise	1.010e-2	4.176e-2	8.765e-3	7.428e-3	Descent from Cruise	4.958e-3	0.000	2.461e-1	1.428e-1
Final Descent	1.370e-2	5.303e-2	1.165e-2	1.022e-2	Final Descent	7.233e-4	0.000	3.457e-4	2.204e-4
Approach	1.483e-2	5.630e-2	1.258e-2	1.110e-2	Approach	5.058e-4	0.000	2.217e-4	1.731e-4
Level Off	1.513e-2	5.716e-2	1.283e-2	1.134e-2	Level Off	4.700e-4	0.000	2.031e-4	1.652e-4
Landing Roll	1.461e-2	5.561e-2	1.238e-2	1.094e-2	Landing Roll	4.870e-4	0.000	2.128e-4	1.737e-4

References

- [1] Owen, B., Lee, D. S., and Lim, L., “Flying into the Future: Aviation Emissions Scenarios to 2050,” *Environmental Science Technology*, Vol. 44, No. 7, 2010. doi:10.1021/es902530z, URL <https://pubs.acs.org/doi/full/10.1021/es902530z>.
- [2] Airbus, “Annual Review 2023,” 2023. URL <https://www.iata.org/contentassets/c81222d96c9a4e0bb4ff6ced0126f0bb/annual-review-2023.pdf>.
- [3] Kärcher, B., “Formation and radiative forcing of contrail cirrus,” *Nature Communications*, Vol. 9, No. 1, 2018, p. 1824. doi:10.1038/s41467-018-04068-0, URL <https://doi.org/10.1038/s41467-018-04068-0>.
- [4] UKRI, “A Brief History of Climate Change Discoveries,” , 2023. URL <https://www.discover.ukri.org/a-brief-history-of-climate-change-discoveries/index.html>, accessed: 2024-11-20.
- [5] Lee, D., Fahey, D., Skowron, A., Allen, M., Burkhardt, U., Chen, Q., Doherty, S., Freeman, S., Forster, P., Fuglestvedt, J., Gettelman, A., De León, R., Lim, L., Lund, M., Millar, R., Owen, B., Penner, J., Pitari, G., Prather, M., Sausen, R., and Wilcox, L., “The contribution of global aviation to anthropogenic climate forcing for 2000 to 2018,” *Atmospheric Environment*, Vol. 244, 2021, p. 117834. doi:10.1016/j.atmosenv.2020.117834, URL <https://doi.org/10.1016/j.atmosenv.2020.117834>.
- [6] Air Transport Action Group, “Tracking Aviation Efficiency,” Accessed via aviationbenefits.org, 2021. URL <https://aviationbenefits.org/downloads/fact-sheet-3-tracking-aviation-efficiency/>, fact Sheet #3.
- [7] Air Transport Action Group, “Waypoint 2050,” , 2020. URL <https://www.atag.org/waypoint-2050>, accessed: 2025-06-09.
- [8] Gharbia, Y., Derakhshandeh, J. F., Alam, M. M., and Amer, A. M., “Developments in Wingtip Vorticity Mitigation Techniques: A Comprehensive Review,” *Aerospace*, Vol. 11, No. 1, 2024, p. 36. doi:10.3390/aerospace11010036, URL <https://doi.org/10.3390/aerospace11010036>.
- [9] Chen, Y., Zhao, Y., and Wu, Y., “Recent progress in air traffic flow management: A review,” *Journal of Air Transport Management*, 2024, p. 102573. doi:10.1016/j.jairtraman.2024.102573, URL <https://doi.org/10.1016/j.jairtraman.2024.102573>.
- [10] Boeing, “2023 Commercial Market Outlook Executive Summary,” , 2023. URL <https://www.boeing.com/content/dam/boeing/boeingdotcom/market/assets/downloads/2023-Commercial-Market-Outlook-Executive-Summary.pdf>.
- [11] Ansell, P. J., “Review of sustainable energy carriers for aviation: Benefits, challenges, and future viability,” *Progress in Aerospace Sciences*, Vol. 141, 2023, p. 100919. doi:<https://doi.org/10.1016/j.paerosci.2023.100919>, URL <https://www.sciencedirect.com/science/article/pii/S0376042123000350>, special Issue on Green Aviation.
- [12] Brink, L. F. J., “Modeling the impact of fuel composition on aircraft engine NOx, CO and soot emissions,” Master’s Thesis, Massachusetts Institute of Technology, Cambridge, MA, 2020.
- [13] Heywood, J. B., and Mikus, T., “Parameters controlling nitric oxide emissions from gas turbine combustors,” Tech. Rep. NASA-CR-132959, NASA Contractor Report, London, England, Apr. 1973. URL <https://ntrs.nasa.gov/citations/19730017094>, presented at the AGARD Propulsion and Energetics Panel 41st Meeting on Atmospheric Pollution by Aircraft Engines, London, England, April 9-13, 1973.
- [14] International Civil Aviation Organization (ICAO), “Annex 16 to the Convention on International Civil Aviation, Volume II: Aircraft Engine Emissions,” <https://www.icao.int/environmental-protection/Pages/Annex-16-Volume-II.aspx>, 2017. URL <https://www.icao.int/environmental-protection/Pages/Annex-16-Volume-II.aspx>, chapter 3: Local Air Quality.
- [15] Blakey, S., Rye, L., and Wilson, C. W., “Aviation gas turbine alternative fuels: A review,” *Proceedings of the Combustion Institute*, Vol. 33, No. 2, 2011, pp. 2863–2885. doi:10.1016/j.proci.2010.09.011, URL <https://doi.org/10.1016/j.proci.2010.09.011>.
- [16] Goodwin, D. G., Speth, R. L., Moffat, H. K., and Weber, B. W., “Cantera: An Object-Oriented Software Toolkit for Chemical Kinetics, Thermodynamics, and Transport Processes,” , 2023. URL <https://www.cantera.org>, version 3.0.0 [Computer software].
- [17] Marathon Technical Services, “Fuel Properties Table,” , n.d. URL <https://www.marathontech.ca/assets/reference-material/fueltbl.pdf>, accessed: 2024-9-24.

- [18] Alaoui, F., Montero, E., Bazile, J. P., Comuñas, M. J. P., Galliero, G., and Boned, C., “Liquid density of 1-butanol at pressures up to 140 MPa and from 293.15 K to 403.15 K,” *Fluid Phase Equilibria*, Vol. 301, No. 2, 2011, pp. 131–136. doi:10.1016/j.fluid.2010.11.020, URL <https://doi.org/10.1016/j.fluid.2010.11.020>.
- [19] Chuck, C. J., and Donnelly, J., “The compatibility of potential bioderived fuels with Jet A-1 aviation kerosene,” *Applied Energy*, Vol. 118, 2014, pp. 83–91. doi:10.1016/j.apenergy.2013.12.019, URL <https://doi.org/10.1016/j.apenergy.2013.12.019>.
- [20] Wang, T., Cao, X., and Jiao, L., “PEM water electrolysis for hydrogen production: fundamentals, advances, and prospects,” *Carbon Neutrality*, Vol. 1, No. 1, 2022, p. 21. doi:10.1007/s43979-022-00022-8.
- [21] Kumar, S. S., and Himabindu, V., “Hydrogen production by PEM water electrolysis—A review,” *Materials Science for Energy Technologies*, Vol. 2, No. 3, 2019, pp. 442–454. doi:10.1016/j.mset.2019.03.002.
- [22] Liu, C. M., Sandhu, N. K., McCoy, S. T., and Bergerson, J. A., “A life cycle assessment of greenhouse gas emissions from direct air capture and Fischer-Tropsch fuel production,” *Sustainable Energy & Fuels*, Vol. 4, No. 6, 2020, pp. 3129–3142. doi:10.1039/C9SE00479C.
- [23] Glebov, L. S., and Kliger, G. A., “The molecular weight distribution of the products of the Fischer-Tropsch synthesis,” *Russian Chemical Reviews*, Vol. 63, No. 2, 1994, p. 185. doi:10.1070/RC1994v06n02ABEH000079.
- [24] Zang, G., Sun, P., Elgowainy, A., Bafana, A., and Wang, M., “Life Cycle Analysis of Electrofuels: Fischer-Tropsch Fuel Production from Hydrogen and Corn Ethanol Byproduct CO₂,” *Environmental Science & Technology*, Vol. 55, No. 6, 2021, pp. 3888–3897. doi:10.1021/acs.est.0c05893.
- [25] Boilley, J. H., Berrady, A., Shahrel, H. B., Gürbüz, E., and Gallucci, F., “Energy analysis of a power-to-jet-fuel plant,” *International Journal of Hydrogen Energy*, Vol. 58, 2024, pp. 1160–1176. doi:10.1016/j.ijhydene.2024.01.262.
- [26] LEADS Group, “RCAIDE: Open-source Python environment for electrified aircraft design,” <https://github.com/leadsgroup/RCAIDE>, 2024. Accessed: 2024-11-13.
- [27] Shekar, S. S., and Clarke, M. A., “Design and In-Flight Analysis of an Electric Aircraft’s Battery Thermal Management System,” *2024 IEEE Transportation Electrification Conference and Expo (ITEC)*, Chicago, IL, USA, 2024, pp. 1–8. doi:10.1109/ITEC60657.2024.10598998.
- [28] “Vortex-Lattice Utilization: A Workshop Held at Langley Research Center, Hampton, Virginia, May 17–18, 1976,” Tech. Rep. NASA CP-405, NRSA-5P-405, NASA, Langley Research Center, Hampton, VA, 1976. NASA Conference Publication, CSCL 31A.
- [29] U.S. Government Printing Office, *U.S. Standard Atmosphere, 1976*, U.S. Government Printing Office, Washington, D.C., 1976.
- [30] Cantwell, B. J., “AA283 Course Reader: Aircraft and Rocket Propulsion,” Unpublished course reader, Jan. 2021. Department of Aeronautics and Astronautics, Stanford University. Course notes, not publicly distributed.
- [31] Goodwin, D. G., Moffat, H. K., Schoegl, I., Speth, R. L., and Weber, B. W., “Cantera: An object-oriented software toolkit for chemical kinetics, thermodynamics, and transport processes,” <https://www.cantera.org>, 2023. doi:10.5281/zenodo.8137090, version 3.0.0.
- [32] Developers, G., “GeoPy: Geocoding library for Python,” <https://geopy.readthedocs.io/en/stable/>, 2024. Accessed: April 13, 2025.
- [33] Raymer, D. P., *Aircraft Design: A Conceptual Approach, Seventh Edition*, American Institute of Aeronautics and Astronautics, Inc., 2024. doi:10.2514/4.107290, URL <http://dx.doi.org/10.2514/4.107290>.
- [34] Moran, J., *An Introduction to Theoretical and Computational Aerodynamics*, reprint edition ed., Dover Books on Aeronautical Engineering, Dover Publications, Mineola, NY, 2003.
- [35] Wells, D. P., Horvath, B. L., and McCullers, L. A., “The Flight Optimization System Weights Estimation Method,” Tech. Rep. NASA/TM-2017-219627/VOL1, NASA Langley Research Center, Hampton, VA, United States, 2017. URL <https://ntrs.nasa.gov/citations/20170005851>, technical Memorandum, NF1676L-27097, L-20820. Public Use Permitted.
- [36] Proesmans, P.-J., and Vos, R., “Airplane Design Optimization for Minimal Global Warming Impact,” *AIAA Scitech 2021 Forum*, American Institute of Aeronautics and Astronautics, 2021. doi:10.2514/6.2021-1297, URL <http://dx.doi.org/10.2514/6.2021-1297>.

- [37] U.S. Bureau of Transportation Statistics, “Bureau of Transportation Statistics,” , 2024. URL <https://www.bts.gov/>, accessed: May 8, 2025.
- [38] De Havilland Aircraft of Canada, “De Havilland Aircraft of Canada,” , 2024. URL <https://dehavilland.com/>, accessed: May 8, 2025.
- [39] ATR Aircraft, “ATR Aircraft Official Website,” , 2024. URL <https://www.atr-aircraft.com/>, accessed: May 8, 2025.
- [40] Embraer Commercial Aviation, “Embraer Commercial Aviation,” , 2024. URL <https://www.embraercommercialaviation.com/>, accessed: May 8, 2025.
- [41] The Boeing Company, “Boeing Official Website,” , 2024. URL <https://www.boeing.com/>, accessed: May 8, 2025.
- [42] GSP Team, “About GSP – Gas Turbine Simulation Program,” , 2024. URL <https://gspteam.com/about.html>, accessed: May 8, 2025.
- [43] Nicolai, L. M., and Carichner, G. E., *Fundamentals of Aircraft and Airship Design*, American Institute of Aeronautics and Astronautics, 2010. ISBN: 978-1-60086-753-8.
- [44] Bisson, J., Seers, P., Huegel, M., and Garnier, F., “Numerical Prediction of Gaseous Aerosol Precursors and Particles in an Aircraft Engine,” *Journal of Propulsion and Power*, Vol. 32, No. 4, 2016, pp. 918–928. doi: 10.2514/1.B35943, URL <https://www.scopus.com/inward/record.uri?eid=2-s2.0-84977109952&doi=10.2514%2f1.B35943&partnerID=40&md5=e704d05d06e3e895ecaad0dadcd217d21>.
- [45] Allaire, D. L., “A physics-based emissions model for aircraft gas turbine combustors,” S.M. Thesis, Massachusetts Institute of Technology, Dept. of Aeronautics and Astronautics, Cambridge, MA, Jun. 2006. URL <https://dspace.mit.edu/handle/1721.1/35584>, advisor: Karen Willcox and Ian Waitz.
- [46] Chowdhury, G. M., and Yu, F., “A 0D aircraft engine emission model with detailed chemistry and soot microphysics,” *Combustion and Flame*, Vol. 159, No. 4, 2012, pp. 1670–1686. doi:10.1016/j.combustflame.2011.11.006, URL <https://doi.org/10.1016/j.combustflame.2011.11.006>.
- [47] Lefebvre, A. H., and Ballal, D. R., *Gas Turbine Combustion: Alternative Fuels and Emissions, Third Edition*, 3rd ed., Taylor & Francis, Boca Raton, FL, 2010.
- [48] European Union Aviation Safety Agency, “ICAO Aircraft Engine Emissions Databank,” , 2024. URL <https://www.easa.europa.eu/en/domains/environment/icao-aircraft-engine-emissions-databank>, accessed: April 9, 2025.
- [49] Norman, P., Lister, D., Lecht, M., Maddén, P., Park, K., Penanhoat, O., Plaisance, C., and Renger, K., “Development of the technical basis for a New Emissions Parameter covering the whole AIRcraft operation: NEPAIR - final Technical Report,” Tech. rep., Europäische Kommission, Sep. 2003. [EuKom03z].
- [50] European Union Aviation Safety Agency, “ICAO Aircraft Engine Emissions Databank,” , 2025. URL <https://www.easa.europa.eu/en/domains/environment/icao-aircraft-engine-emissions-databank>, accessed: April 9, 2025.